

## Article

# Genesis of the Dongtangzi Zn-Pb Deposit of the Fengxian–Taibai Ore Cluster in West Qinling, China: Constraints from Rb-Sr and Sm-Nd Geochronology, and In Situ S-Pb Isotopes

Qiaoqing Hu <sup>1</sup>, Yitian Wang <sup>1,\*</sup> , Shaocong Chen <sup>2</sup>, Ran Wei <sup>1</sup>, Xielu Liu <sup>3</sup>, Junchen Liu <sup>4</sup>, Ruiting Wang <sup>5</sup>, Weihong Gao <sup>5</sup>, Changan Wang <sup>6</sup>, Minjie Tang <sup>6</sup> and Wentang Wu <sup>6</sup>

- <sup>1</sup> MNR Key Laboratory of Metallogeny and Mineral Assessment, Institute of Mineral Resources, Chinese Academy of Geological Sciences, Beijing 100037, China; huqiaoqing@cags.ac.cn (Q.H.); weiranyspa@126.com (R.W.)
- <sup>2</sup> MNR Key Laboratory for Polar Science, Polar Research Institute of China, Ministry of Natural Resources, Shanghai 200136, China; shaocong0211@163.com
- <sup>3</sup> Beijing Institute of Exploration Engineering, Beijing 100083, China; liuxielu@mail.cgs.gov.cn
- <sup>4</sup> Collaborative Innovation Center for Exploration of Nonferrous Metal Deposits and Efficient Utilization of Resources by the Province and Ministry, Guilin University of Technology, Guilin 541004, China; ljccugb@163.com
- <sup>5</sup> Northwest Nonferrous Geological and Mining Group Co., Ltd., Xi'an 710054, China; wrtyf@163.com (R.W.); 717gwh@163.com (W.G.)
- <sup>6</sup> Baoji No.717 Corps Limited of Northwest Nonferrous Geological and Mining Group, Baoji 721015, China; wangchangan1463@163.com (C.W.)
- \* Correspondence: wyt69@263.net



**Citation:** Hu, Q.; Wang, Y.; Chen, S.; Wei, R.; Liu, X.; Liu, J.; Wang, R.; Gao, W.; Wang, C.; Tang, M.; et al. Genesis of the Dongtangzi Zn-Pb Deposit of the Fengxian–Taibai Ore Cluster in West Qinling, China: Constraints from Rb-Sr and Sm-Nd Geochronology, and In Situ S-Pb Isotopes. *Minerals* **2024**, *14*, 297. <https://doi.org/10.3390/min14030297>

Academic Editor: George M. Gibson

Received: 27 December 2023

Revised: 11 February 2024

Accepted: 6 March 2024

Published: 12 March 2024



**Copyright:** © 2024 by the authors. Licensee MDPI, Basel, Switzerland. This article is an open access article distributed under the terms and conditions of the Creative Commons Attribution (CC BY) license (<https://creativecommons.org/licenses/by/4.0/>).

**Abstract:** The large Dongtangzi Zn-Pb deposit is located in the southwest of the Fengxian–Taibai (abbreviated as Fengtai) ore cluster in the west Qinling orogen. The origin of the deposit is controversial, positing diverse genesis mechanisms such as sedimentary-exhalative (SEDEX), sedimentary-reformed, and epigenetic-hydrothermal types. This study combines systematic ore geology observations with high-precision Rb-Sr and Sm-Nd ages of 211 Ma and in situ S-Pb isotopes to constrain the timing and origin of mineralization. In situ S-Pb isotopic studies show that the sulfide ores display a narrow range of  $\delta^{34}\text{S}$  values from 1.1‰ to 10.2‰, with  $^{206}\text{Pb}/^{204}\text{Pb}$ ,  $^{207}\text{Pb}/^{204}\text{Pb}$ , and  $^{208}\text{Pb}/^{204}\text{Pb}$  ratios of 18.07 to 18.27, 15.64 to 15.66, and 38.22 to 38.76, respectively. On the other hand, pyrites of the sedimentary period and the granite porphyry dike have  $\delta^{34}\text{S}$  values ranging from 15.8 to 21.4‰ and from 2.1 to 4.3‰ (with  $^{206}\text{Pb}/^{204}\text{Pb}$  ratios of 18.09 to 18.10,  $^{207}\text{Pb}/^{204}\text{Pb}$  ratios of 15.59 to 15.61, and  $^{208}\text{Pb}/^{204}\text{Pb}$  ratios of 38.17 to 38.24), respectively. The above-mentioned S-Pb isotopic compositions indicate that the metallic materials involved in ore formation originated from a mixture of Triassic magmatic hydrothermal fluid and metamorphic basement. By integrating the regional geology, mineralization ages, and S-Pb isotopic studies, we propose that the Dongtangzi Zn-Pb deposit is the product of epigenetic hydrothermal fluid processes, driven by Late Triassic regional tectono-magmatic processes.

**Keywords:** Rb-Sr and Sm-Nd isotopic dating; in situ S-Pb isotopes; ore genesis; Zn-Pb deposit; Dongtangzi; west Qinling orogen

## 1. Introduction

The Fengxian–Taibai (abbreviated as “Fengtai”) ore cluster, located in the west Qinling orogen, forms part of the giant Qinling Pb-Zn-Au metallogenic belt, which is itself a subsidiary component of the Qinling orogenic belt. Several large and medium-sized Zn-Pb deposits are present, including, from west to east, the Fengya, Yindongliang, Qiandongshan–Dongtangzi, Bafangshan–Erlihe, and Yinmusi deposits, along with many other small-sized deposits and occurrences. Moreover, there are two large Au deposits, known as Baguamiao

and Shuangwang, along with many small-sized Au deposits, and several small Cu deposits. The total reserve contains over 5 Mt of Pb + Zn and there is more than 200 t of gold in the ore cluster [1,2]. The large Dongtangzi Zn-Pb deposit, located in the southwest of the Fengtai ore cluster (Figure 1), contains over 1.5 Mt of Pb + Zn, with an average grade of 7.7 wt% Zn and 1.7 wt% Pb [3]. The Dongtangzi Zn-Pb deposit was discovered in the late 1950s and was formerly known as the Qiandongshan deposit. Around 2002, the newly discovered, concealed west area of the Qiandongshan main ore body was called the Dongtangzi mine section. After the year 2004, the two mine sections were merged under one name and collectively called the Dongtangzi Zn-Pb deposit. Previous research work has mainly focused on the Qiandongshan mine section, while less work has been carried out on the Dongtangzi mine section. Since the 1980s, extensive investigations have been conducted into the Dongtangzi Zn-Pb deposit to understand its geological characteristics and ore-controlling structures [3–6], stable isotope and trace element geochemistry [7–11], and ore genesis [5,11–17]. Despite decades of research, the origin of the ore remains contentious.

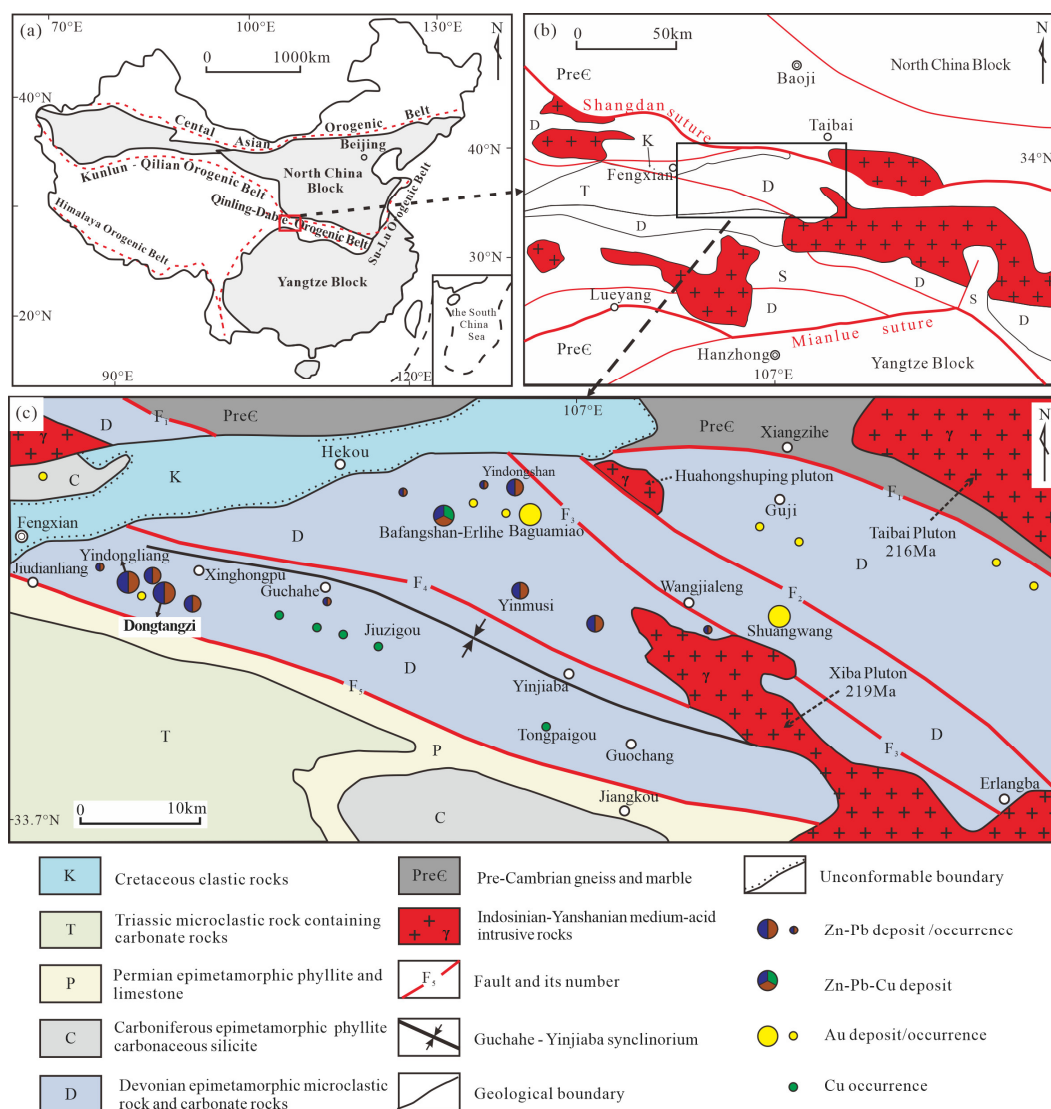


**Figure 1.** Sketch maps of (a) tectonic units of China and (b) west Qinling orogenic belt, along with a geological map of (c) the Fengxian–Taibai (abbreviated as “Fengtai”) ore cluster (modified from Wang X. et al., 1996; Hu Q.Q. et al., 2020 [18,19]). Notes: F<sub>1</sub>: Xiangzihe–Huangbaiyuan Fault (Shang-Dan suture zone); F<sub>2</sub>: Xiushiyan–Guanyinxia Fault; F<sub>3</sub>: Wangjialeng–Erlangba Fault; F<sub>4</sub>: Daohuigou–Zheliyuan Fault; F<sub>5</sub>: Jiudianliang–Jiangkou Fault.

Many researchers [5,15,20] believe that it is a sedimentary exhalative (SEDEX) deposit developed in the Devonian period. Others contend that it is of epigenetic origin [3,16–18,21] and a product of Triassic tectonic–hydrothermal processes. Due to the lack of precise geochronology data and comprehensive isotopic geochemistry studies, particularly the lack of in situ technique analysis, the metallogenic processes of the Dongtangzi Zn–Pb deposit remain poorly understood. Therefore, this study presents a comprehensive identification of its deposit geology, along with Rb–Sr and Sm–Nd geochronology and in situ S–Pb isotopic studies, aiming to further constrain the genesis of the Dongtangzi Zn–Pb deposit. The new results in this study, provide valuable information about the timing of Zn–Pb mineralization and the source of ore-forming materials. They also allow us to refine the origin of the Dongtangzi Zn–Pb deposit, which will be an essential factor for understanding the Zn–Pb metallogeny throughout the entire Fengtai ore cluster and the west Qinling Zn–Pb belt.

## 2. Regional Geology

The Qinling orogen was formed during the convergence and collision of the North China and Yangtze blocks (Figure 1a), resulting in a multi-stage composite orogenic belt composed of two suture zones and three tectonic belts [22]. The three tectonic units are, from north to south, the North Qinling belt, the South Qinling belt, and the north margin of the Yangtze block [22]. The northern suture zone is the Early Silurian Shangdan suture (Figure 1b), and the southern is the Late Triassic Mianlue suture (Figure 1b). The Fengtai ore cluster is located in the middle-west of the South Qinling belt (Figure 1c), which is bordered by the NWW-trending faults of the Xiangzihe–Huangbaiyuan fault ( $F_1$ , part of the Shangdan suture) in the north and the Jiudianliang–Jiangkou fault ( $F_5$ ) in the south (Figure 1c). There are three NWW-trending faults inside the ore cluster called the Xiushiyan–Guanyinxia ( $F_2$ ), Wangjialeng–Erlangba ( $F_3$ ), and Daohuigou–Zheliyuan ( $F_4$ ) faults (Figure 1c). The basic tectonic setting of the Fengtai ore cluster is a compound fold with well-developed secondary folds and faults. The tectonic style is a large-scale transpressional strike–slip duplex system resulting from regional sinistral strike–slip faulting [23].

The Fengtai ore cluster is hosted by Middle–Upper Devonian siliciclastic and carbonate rocks (Figure 1c) deposited in a littoral–neritic depositional environment and subsequently metamorphosed under low greenschist facies conditions. This vertical succession comprises, from bottom to top, fine clastic rocks and metasandstone of the Middle Devonian Macaogou Formation ( $D_2m$ ), followed by carbonate rocks of the Middle Devonian Guadaoling Formation ( $D_2g$ ), clastic–carbonate rocks of the Upper Devonian Xinghongpu Formation ( $D_3x$ ), and fine clastic rocks of the Upper Devonian Jiuliping Formation ( $D_3j$ ). Around the periphery of the ore cluster, high-grade meta-sedimentary rocks and volcanic rocks of the Proterozoic Qinling Group ( $Pt_1q$ ) and Danfeng Group ( $Pt_1d$ ) appear to the north; carbonate and clastic rocks of the Lower Carboniferous ( $C_1$ ) period and breccia with siltstone of the Lower Cretaceous ( $K_1$ ) period appear to the northwest (Figure 1c); and marine carbonate rocks with continental clastic rocks of the Carboniferous (C) period and limestone of the Lower Triassic Liufengguan Group ( $T_1l$ ) appear to the southwest (Figure 1c).

Intense Triassic magmatic activity has been recorded in the ore cluster. The Xiba intermediate–felsic pluton, trending NWW, is positioned to the southeast of the cluster (Figure 1c), comprising medium-fine-grained granodiorite, monzogranite, quartz diorite, and tonalite, with transitional contact relations. A small Huahongshuping granodioritic intrusive stock is located in the north (Figure 1c). In addition, numerous dikes of diorite, granite porphyry, and lamprophyre commonly develop throughout the ore cluster (mainly concentrated adjacent to the Pb–Zn and Au deposits), filling the NE- or NWW-trending faults, with a thickness of tens of centimeters to several meters.

### 3. Ore Deposit Geology

#### 3.1. Structures

The “M”-shaped Qiandongshan–Dongtangzi brachyanticline is the principal ore-hosting structure, striking about 280° (Figure 2). The hinge of the anticline plunges westwards at angles between 27° and 37°. There are EW-, NW-, and NE-trending faults in the mine area. The EW-trending reverse faults are the largest in scale and are developed mostly in the interface between the Gudaoling Formation and Xinghongpu Formation (Figure 2). The NW- and NE-trending faults are of smaller size but more abundant, belonging to the “X”-type conjugate shear faults formed under regional shearing events, cutting through the main orebody with small fault displacements.

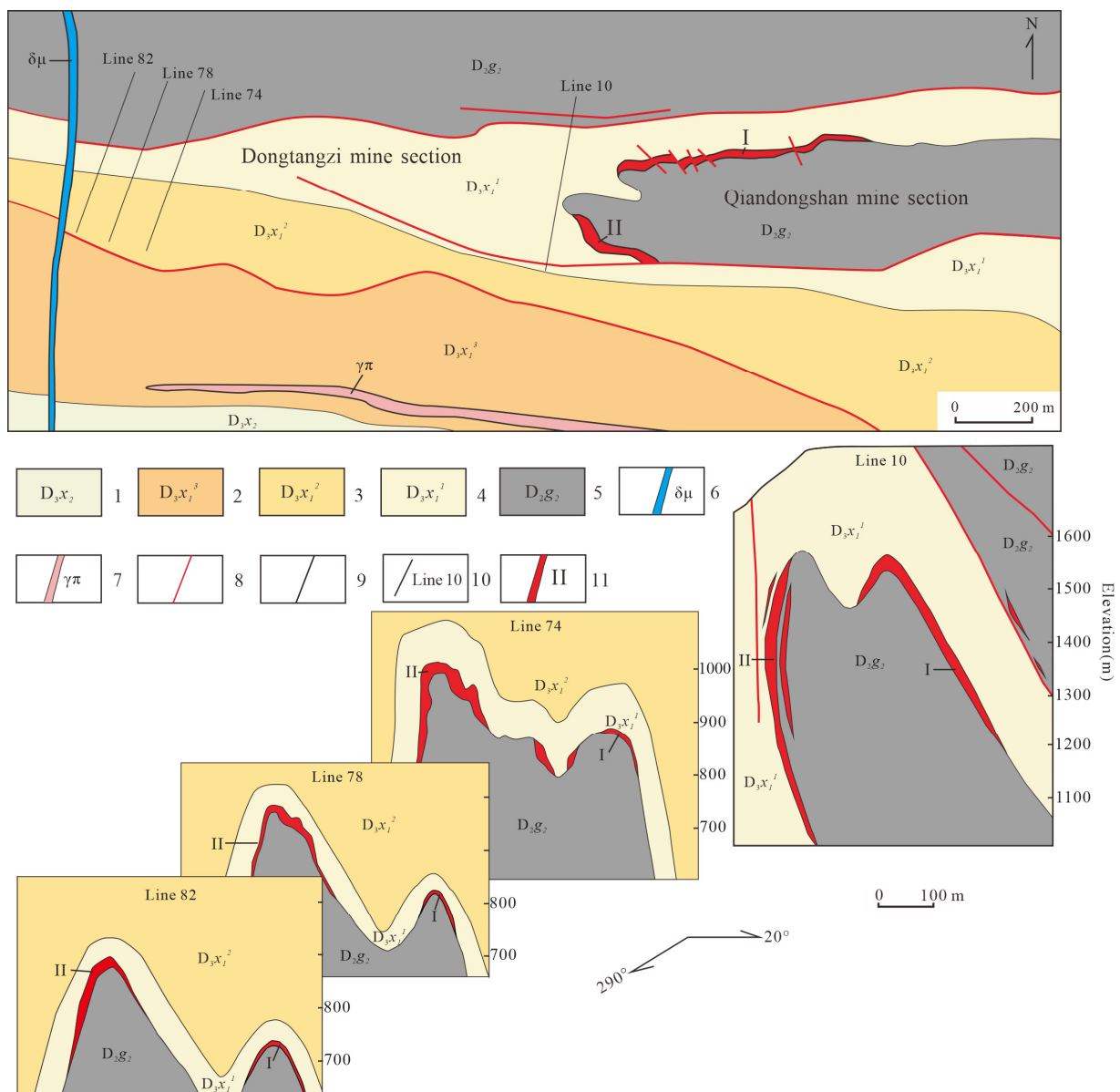


**Figure 2.** Geological map and composite cross-sections of the Dongtangzi Zn-Pb deposit (after Qi et al., 1993; Tang, 2013; Wu et al., 2016; Wang et al., 2023 [3,15,24]). Note: 1. The Upper Section of the Xinghongpu Formation (D<sub>3</sub>x<sub>2</sub>); 2. Upper member of the Lower Section of Upper Devonian Xinghongpu Formation (D<sub>3</sub>x<sub>1</sub><sup>3</sup>); 3. Middle member of the Lower Section of Upper Devonian Xinghongpu Formation

( $D_3x_1^2$ ); 4. Lower member of the Lower Section of Upper Devonian Xinghongpu Formation ( $D_3x_1^1$ ); 5. The Upper Section of the Middle Devonian Gudaoling Formation ( $D_2g_2$ ); 6. Diorite porphyry dike; 7. Granite porphyry dike; 8. Fault; 9. Geological boundary; 10. Prospecting line and its number; 11. Zn-Pb orebody and its number.

### 3.2. Rocks

The strata within the mine area contain the Upper Section of the Middle Devonian Gudaoling Formation ( $D_2g_2$ ) and the Upper Devonian Xinghongpu Formation ( $D_3x$ ) (Figure 2). The EW-striking upper section of the Gudaoling Formation hosts the main orebody (Figures 2 and 3), which is comprised of microcrystalline biolithite and carbonaceous microcrystalline limestone, intensively silicified at the top by meters to tens of meters in thickness. The Xinghongpu Formation is comprised of two lithologic sections, namely the Lower Section ( $D_3x_1$ ) and the Upper Section ( $D_3x_2$ ), respectively. The Lower Section ( $D_3x_1$ ) is comprised of three members, including the lower ( $D_3x_1^1$ ) ferrodolomitic phyllite with sericite phyllite and thin layers of carbonaceous limestone, the middle ( $D_3x_1^2$ ) ferrodolomitic phyllite with thin layers of limestone and silty sericite phyllite, and the upper ( $D_3x_1^3$ ) carbonaceous phyllite with thin layers of carbonaceous biolithite. Among them, the carbonaceous limestone of the lower member ( $D_3x_1^1$ ) hosts a small scale of Zn-Pb orebody (Figure 3). The Upper Section ( $D_3x_2$ ) consists mainly of chlorite sericite phyllite, with less ferrodolomitic sericite phyllite at the bottom (Figure 3).

Rock units	Strata column	Lithologic description
The Upper section of the Upper Devonian Xinghongpu Formation ( $D_3x_2$ )		Chlorite sericite phyllite, unmineralized, with thickness about 200 m
Upper member of the Lower section of the Upper Devonian Xinghongpu Formation ( $D_3x_1^3$ )		Carbonaceous calcareous sericite phyllite with thin layer of carbonaceous biolithite, unmineralized, with thickness about 300 m
Middle member of the Lower section of the Upper Devonian Xinghongpu Formation ( $D_3x_1^2$ )		Ferrodolomitic phyllite with thin layer of limestone and silty sericite phyllite, unmineralized, with thickness about 200 m
Lower member of the Lower section of the Upper Devonian Xinghongpu Formation ( $D_3x_1^1$ )		Ferrodolomitic phyllite in the top, thin layer of carbonaceous limestone, sericite phyllite in the middle, with Zn-Pb mineralization in the bottom, with thickness about 100 m
The Upper Section of the Middle Devonian Gudaoling Formation ( $D_2g_2$ )		Thick layered carbonaceous bioclastic limestone with calcareous phyllite and sericite carbonaceous phyllite in the top, containing the main Zn-Pb orebody; Thin layered fine grained limestone in the lower part with Zn-Pb mineralized veins, with thickness about 600 m

**Figure 3.** Stratigraphic column of the Dongtangzi Zn-Pb deposit. The thickness of the lithologic section is from Wang J.L. et al., 1996 [5].

The intrusive dikes occur throughout the mine area. There are several diorite porphyry dikes and granite porphyry dikes, filling the NE-trending and NWW-trending faults, respectively. The diorite porphyry dikes crosscut the main orebody, while the granite porphyry dikes—with zircon U-Pb ages of 226~221 Ma (LA-ICP-MS; [25])—are roughly parallel to the main orebody (Figures 3 and 4a). The main minerals of the granite porphyry dikes are plagioclase (30%), potash feldspar (35%), quartz (30%), biotite (3%), pyrite, zircon,

sphene, etc. (Figure 4b,c). The existence of cataclastic quartz suggests that the dike was deformed after its emplacement (Figure 4b,c).

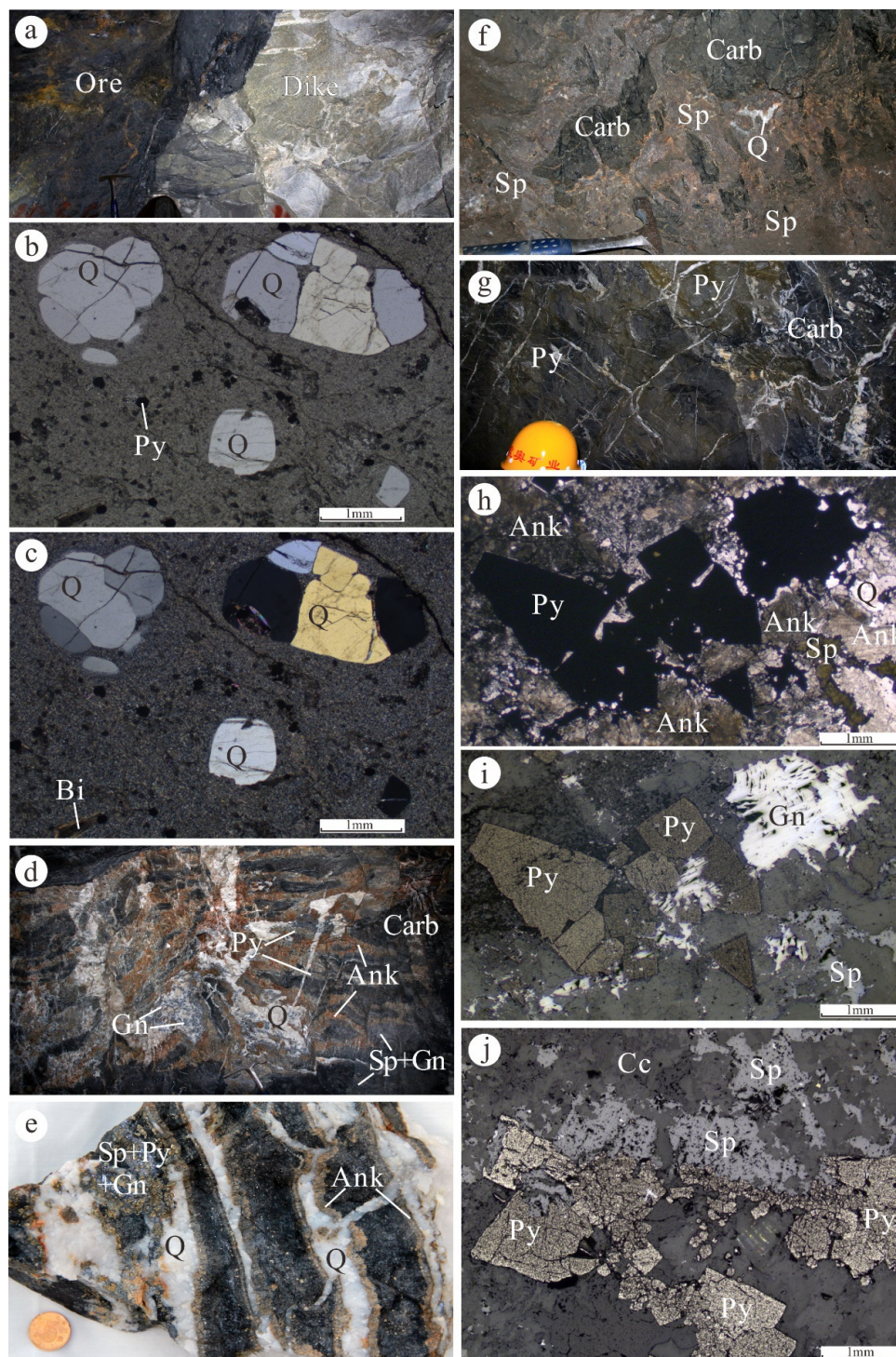


**Figure 4.** Rocks of the Dongtangzi Zn-Pb deposit. (a) The NWW-trending granite porphyry dike crosscutting the main orebody. (b,c) Subhedral granular quartz phenocrysts in the granite porphyry ((b): plane-polarized light; (c): cross-polarized light). (d) Breccia type ore. The brecciated carbonaceous limestone with disseminated sulfides inside and ankerite at the edges, cementing by medium-coarse-grained aggregates of quartz-dolomite-polymetallic sulfides. (e) Veinlet ore. Quartz-sulfide-ankerite veins crosscut the brecciated carbonaceous limestone. (f) Sphalerite-rich massive ore cement the breccia

of dolomitized rocks. (g) Pyrite-rich massive ore with metasomatic remnant of altered carbonates. (h,i) The euhedral granular pyrite was metasomatized by sphalerite and galena within the pyrite-rich ore ((h)—plane-polarized light; (i)—reflected light). (j) The fragmented pyrite metasomatized by sphalerite (reflected light). Abbreviations: Sp—sphalerite; Gn—galena; Py—pyrite; Q—quartz; Ank—ankerite; Cc—calcite; Carb—carbonate.

### 3.3. Orebodies

Controlled by the Qiandongshan–Dongtangzi anticline, the main orebody occurs at the contact zone between the Devonian Gudaoling Formation ( $D_2g$ ) and the Xinghongpu Formation ( $D_3x$ ) (Figures 2 and 3), which is composed of the No.1 orebody (north subsidiary anticline) and the No.2 orebody (south subsidiary anticline), accounting for more than 90% of the total Zn-Pb reserves. The No.1 orebody extends by 2.35 times its depth [26]. The other orebodies occur within the fault fracture zones and irregular tensile fractures in limestone, or within interlayer fractures in phyllite, on a relatively small scale with unstable occurrences (Figures 2 and 3). The eastern part of the No.1 orebody occurs in the northern flank of the anticline and the saddle of the northern subsidiary anticline, and there is a trend of pinching out westward (Figure 2). The No. 2 orebody, located on the southern flank of the anticline, is larger in scale in the west part within the Dongtangzi mine section (Figure 2). The orebodies in the north flank of the anticline are thinner and the wall rocks are strongly foliated, while the orebodies in the south flank of the anticline are thicker, without the preservation of any foliated structures. In addition, within the carbonaceous limestone near the footwall of the No. 2 orebody, a cryptoexplosive breccia pipe was discovered, with different sizes of angular–sub-angular breccias, composed of granite porphyry, quartz vein, altered rock, and massive sulfide ore, cemented with argillaceous and carbonaceous mineral aggregates (Figure 5a).

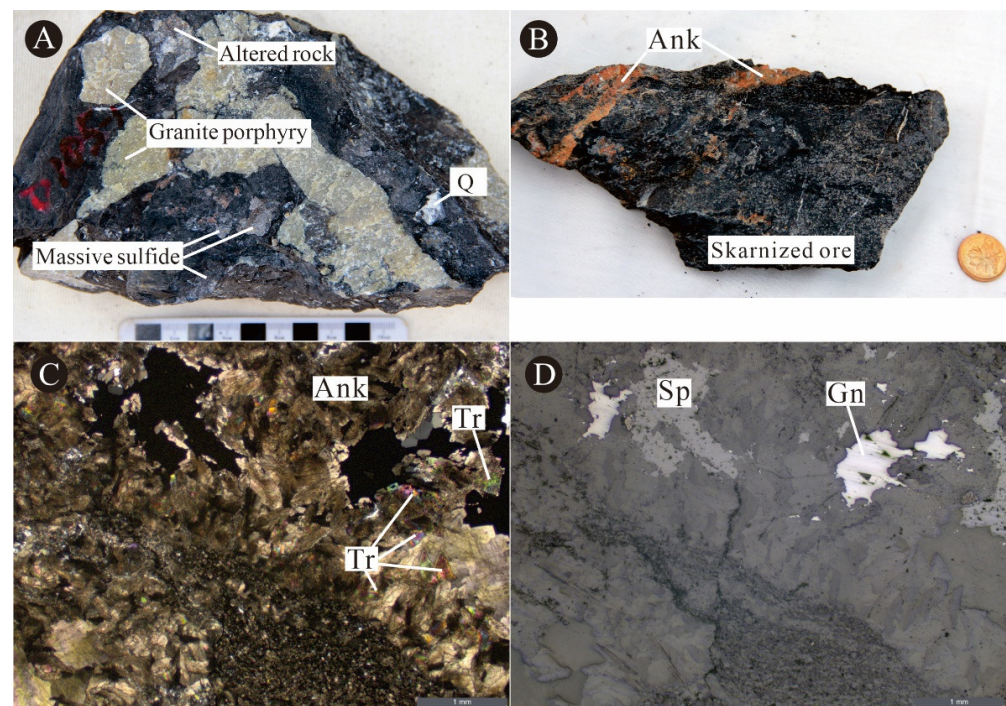


**Figure 5.** Cryptoexplosive breccia and skarn in the Dongtangzi Zn-Pb deposit. (A) Cryptoexplosive breccias, with different sizes of angular–sub-angular breccias, composed of altered granite porphyry, quartz aggregate, altered carbonaceous limestone, and massive sulfide ores, cemented by argillaceous

and carbonaceous mineral aggregates; (B) brecciated ore beside the granite porphyry dike; (C,D) ankerite is replaced by tremolite, which occurs at the edge of fine-grained disseminated sphalerite and galena aggregate ((C): cross-polarized light; (D): reflected light). Note: Sp—sphalerite; Q—quartz; Gn—galena; Ank—ankerite; Tr—tremolite.

The ore minerals mainly comprise sphalerite, galena, pyrite, chalcopyrite, and arsenopyrite. The gangue minerals include quartz, ankerite, dolomite, calcite, siderite, sericite, chlorite, and apatite. The ore structures are mainly veinlets (Figure 4e), banded, brecciated (Figure 4d,f), blocky (Figure 4g), banded, and disseminated. Extensive vein filling and metasomatic mineralization can be observed in all the orebodies. The ore textures include granular (Figure 4h,i), metasomatic (Figure 4h–j), fragmented (Figure 4j), and wrinkling pressure shadow texture. The wall rock alteration is widely and intensively developed throughout the floor and roof rocks, including silicification, dolomitization, calcitization, pyritization, sericitization, and graphitization. In addition, tremolitization is developed in the ore beside the granite porphyry dikes (Figure 5b–d).

3.4. Mineralogy Assemblage and Paragenetic Sequence

Based on a systematic observation of the mineral assemblages, ore structure and texture, hydrothermal alteration, and crosscutting relationships of the multistage veins in the Dongtangzi Zn-Pb deposit, the paragenetic association can be divided into two periods, namely the sedimentary period and the hydrothermal mineralization period. The hydrothermal mineralization period can be further divided into three stages (Figure 6): Stage I, a polymetallic sulfide–ankerite–quartz stage; Stage II, a quartz–pyrite-rich sulfide–ankerite stage; and stage III, a quartz–carbonate–sulfide stage.

Minerals \ Period / Stage	Sedimentary period	Hydrothermal mineralization period		
		Stage I	Stage II	Stage III
Pyrite	—	—————	—————	—————
Dark fine-grained sphalerite		—————	—————	
Light fine-grained sphalerite			—————	—————
Light medium-coarse sphalerite			—————	—————
Galena		—————	—————	
Chalcopyrite		—————	—————	
Tetrahedrite		—————	—————	
Arsenopyrite			—————	—————
Quartz	—	—————	—————	—————
Siderite		—————	—————	
Ankerite	—	—————	—————	
Calcite	—		—————	—————
Fluorite			—————	—————

Figure 6. Mineral paragenetic sequence of the Dongtangzi Zn-Pb deposit.

3.4.1. Sedimentary Period

There is no obvious Zn-Pb mineralization in the sedimentary period, and syn-sedimentary pyrites (Py<sub>0</sub>) are observed, which are mostly metasomatized by sulfides and quartz during the hydrothermal period (Figure 7a–c). The primary sedimentary textures are mostly destroyed by the structural deformation and metamorphism; syngenetic minerals are largely replaced, deformed, and cemented by hydrothermal minerals during the hydrothermal mineralization period.

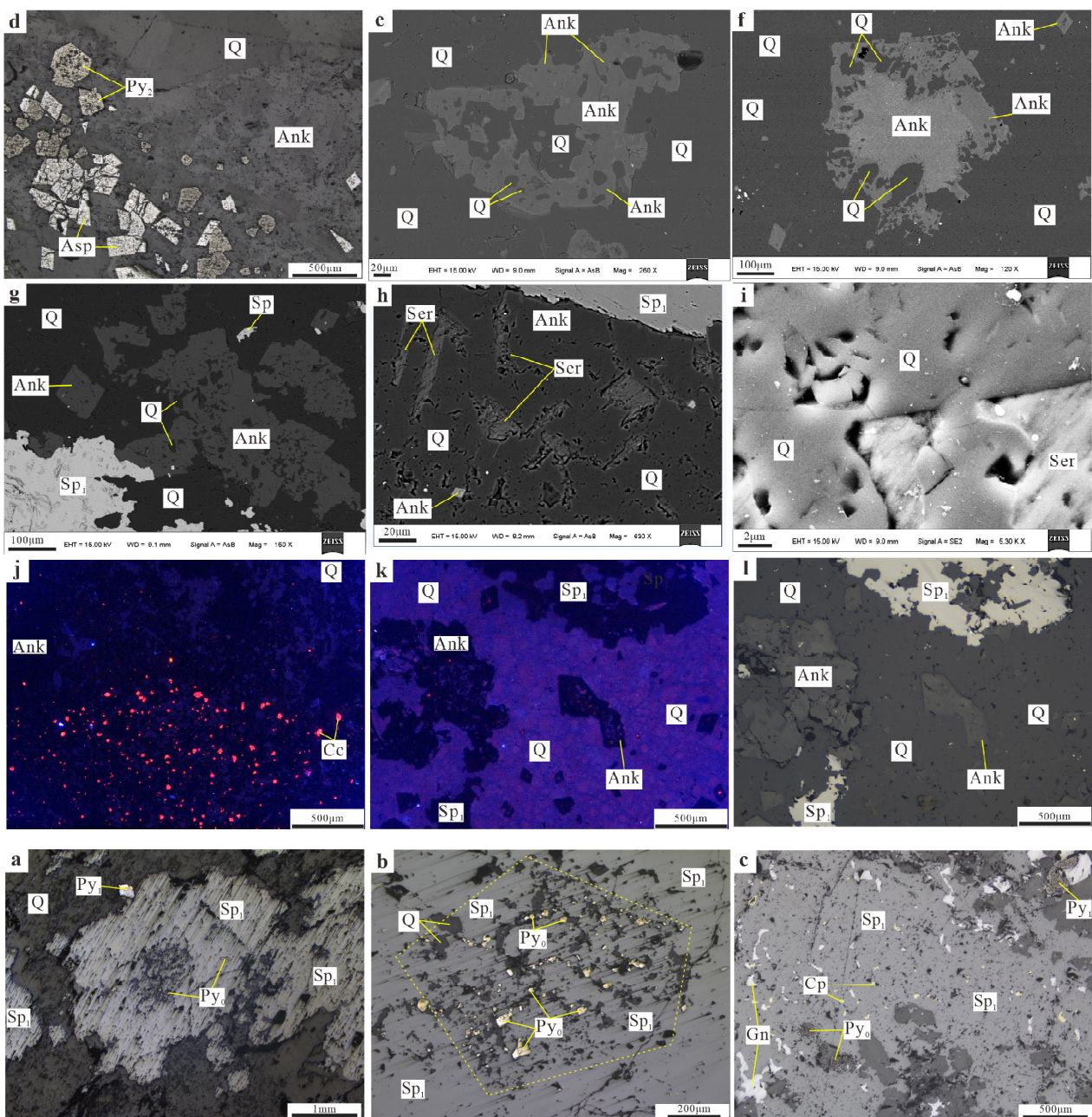


**Figure 7.** Microfabric characteristics of the ore in the Dongtangzi Zn-Pb deposit. (a,b) Metasomatic residual skeleton texture of pyrite ( $Py_0$ ) replaced by the Stage I sphalerite ( $Sp_1$ ), under reflected light. (c) Droplet chalcopyrite (Cp), irregular galena (Gn), and metasomatic residual  $Py_0$  are developed in the massive sphalerite ( $Sp_1$ ), under reflected light. (d) Densely disseminated pyrite ( $Py_2$ ) + arsenopyrite ( $Asp_2$ ) developed in the ferrodolomite siliceous rock, under reflected light. (e,f) The ankerite in the siliceous rock is replaced by quartz, forming skeletal crystal texture, back-scattered electron (BSE) image. (g) Ankerite (Ank) in the siliceous rocks are metasomatized by quartz (Q) and sphalerite, BSE image. (h) Micro-fine aggregates of quartz, sericite (Ser), and ankerite in the siliceous rocks, with sphalerite filling in cracks, BSE image. (i) Scanning electron microscopy (SEM) images show that the surface of the quartz developed triangular pores, with tightly cemented grains, flat edges, and crystal textures. (j) Cathode luminescence (CL) image of the ankerite siliceous rock. The residual of metasomatized calcite is orange colored, while the ankerite is black, and the quartz is deep bluish purple. (k,l) The silicate rocks are metasomatized by quartz and sphalerite ((k)—cathode luminescence, (l)—reflected light).

### 3.4.2. Hydrothermal Mineralization Period

#### Stage I: A Polymetallic Sulfide–Ankerite–Quartz Stage

Stage I is rich in sphalerite and galena, with locally enriched pyrite, accompanied by less chalcopyrite, and is mainly hosted by silicified carbonaceous limestone. The sphalerite is fine-grained and mainly dark brown in color. The galena and pyrite are also fine-grained, cementing the breccia of the carbonaceous altered rock (Figure 8a). The Stage I ore developed silicification, dolomitization, chloritization, and local sericitization, replacing the banded marl along the bedding, or filling the tension fractures within the carbonaceous limestone (Figure 8g). Carbonates are extensively metasomatized by quartz and sulfides (Figure 7e–g), and some quartz and sulfides retain the skeletal crystal structure of carbonates (Figure 7e,f). Stage I is the main mineralization stage, which is generally affected by later tectonic deformation, developing fragmentation and local recrystallization (Figures 4d, 7f and 8a).

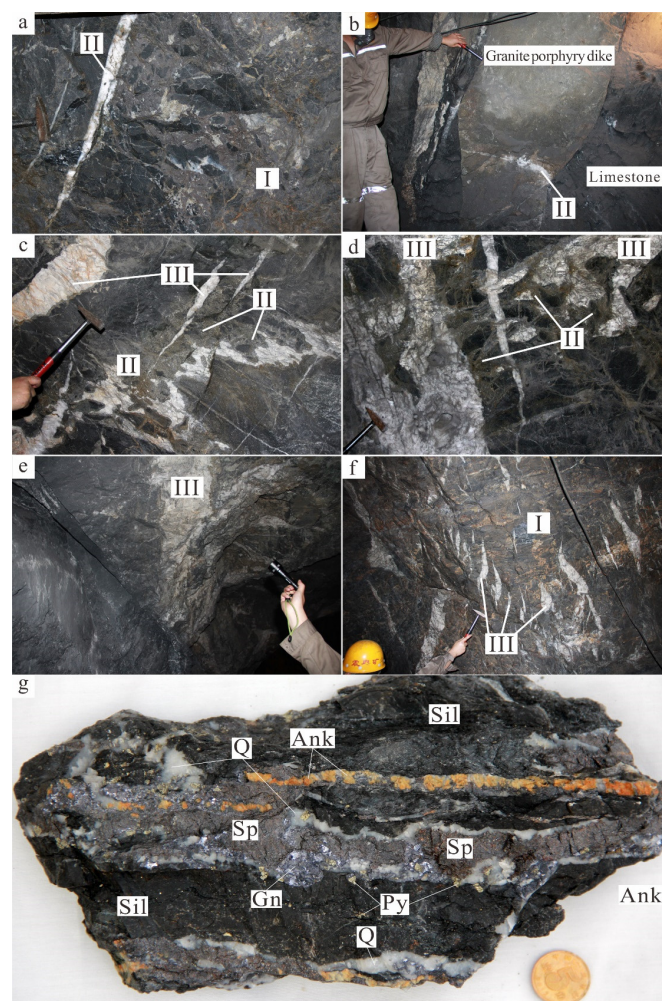


**Figure 8.** Ore of the different mineralization stages in the Dongtangzi Zn-Pb deposit. (a) The Stage I massive and brecciated ores intersected by the Stage II quartz–pyrite–ankerite veins. (b) The granite porphyry dike is crosscut by the Stage II quartz–pyrite–sphalerite vein. (c) The Stage II pyrite-rich ore is crosscut by Stage III quartz–calcite veins. (d) The Stage II pyrite–ankerite vein is crosscut by the Stage III calcite veins. (e) The Stage III coarse-grained calcite–pyrite vein. (f) The Stage III quartz–pyrite–sphalerite veins are arranged in echelon, crosscutting the Stage I ores. (g) The Stage I quartz–sphalerite–galena–pyrite–ankerite parallel veins crosscutting the carbonaceous altered rocks. Note: Sp: sphalerite; Q: quartz; Gn: galena; Ank: ankerite; Sil: siliceous rock.

No obvious sedimentary mineralization characteristics have been found in the ore of the Dongtangzi Zn-Pb deposit. The sheet-like sericite among the quartz grains is irregular (Figure 7h), without obvious orientation, and does not have the typical sedimentary texture of the directional arrangement of argillaceous minerals. The quartz grains are crystalline and there is tight cementation between grains (Figure 7i), with no obvious rounded grain texture, showing no syn-sedimentary characteristics, thereby indicating that the quartz in the altered rocks may occur as a result of hydrothermal fluid running through fracture systems of different scales. Most of the quartz in the altered rocks was obviously formed by metasomatism, as the calcite (the orange region in Figure 7j) is replaced by ankerite (the black region in Figure 7j) and quartz (the blue-purple region in Figure 7j), while the ankerite (Figure 7k,l) is replaced by quartz (the blue-purple region in Figure 7k) and sphalerite (Figure 7k,l). All of the above evidence suggests that the altered rocks were formed by epigenetic hydrothermal replacement of carbonate rocks, rather than by the sedimentary-exhalative processes suggested by some researchers [8,15,27,28].

#### Stage II: A Quartz–Pyrite-rich Sulfide–Ankerite Stage

The Zn-Pb mineralization scale of Stage II is smaller than that of Stage I, but is more enriched in pyrite, which locally intersects and replaces the Stage I ore, silicified carbonaceous limestone (Figure 8a), and silicified phyllite. Meanwhile, the granite porphyry dikes with scattered pyritization are crosscut by the stage II quartz vein (Figure 8b). The quartz–pyrite–ankerite veins are accompanied by polymetallic sulfides such as sphalerite, galena, chalcopyrite, and arsenopyrite, which are generally coarse-grained. The color of the Stage II sphalerite is obviously lighter than that of Stage I, being light yellowish brown in color, and medium-to-fine-grained. According to the interspersed relationship, the NWW-trending granite porphyry dike locally crosscuts the Stage I orebody and is cut through by the quartz–sulfide vein of Stage II, indicating that it was emplaced at a time between Stages I and II. No apparent replacement can be observed on the pyrite (Py<sub>2</sub>) and arsenopyrite (Asp<sub>2</sub>) in the altered rocks (Figure 7d). Dolomitization, pyritization, and silicification are well-developed in the wall rocks during Stage II (Figure 8c,d).

#### Stage III: A Quartz–Carbonate–Sulfide Stage

The Stage III quartz–carbonate–sulfide veins are widely developed in the whole deposit, forming NE-trending joint veins or en echelon veins (Figure 8f), hosted by carbonaceous limestone and phyllite. They mainly consist of coarse-grained quartz and calcite (Figure 8e), with coarse-to-medium-grained ankerite, pyrite, galena, and sphalerite. The Stage III veins are small in scale, which crosscut the wall rocks and the ore veins of the first two stages (Figure 8c,d). The wall rock alteration is weak, including silicification, pyritization, and carbonation.

### 4. Samples and Analytical Methods

All samples utilized in this work were collected from underground tunnels at diverse depths within the Dongtangzi Zn-Pb deposit. After making the polished thin sections, comprehensive microscopic observation was carried out to preliminarily characterize the morphology, textures, and paragenesis of ore-related minerals. Subsequently, representative samples were chosen for further analyses (Table 1). A subset of these samples underwent crushing, with sulfide minerals, including sphalerite, galena, and pyrite, meticulously hand-picked under a binocular microscope. The purity of individual mineral separations exceeded 99%, and all mineral isolations underwent thorough cleaning in an ultrasonic bath. Concurrently, other portions of the samples were polished into thin sections, facilitating high-precision in situ LA-MC-ICP-MS sulfur and lead isotope analyses.

**Table 1.** Samples description of the Dongtangzi Zn-Pb deposit.

No.	Sample	Position	Stage	Type	Description
1	D216.3-1	960 m elevation, north-south of the No.2 ore body	I	Siliceous rock	Siliceous rock with pyrite of the sedimentary period, intersected by the hydrothermal Stage I quartz-pyrite-galena veins
2	D22	1010 m elevation, south flank of the No.2 ore body	I	Disseminated ore	Lamellar carbonaceous altered rock, with disseminated medium-fine grained sphalerite
3	D28-4	960 m elevation, south flank of the No.2 ore body	I	Banded ore	Fine-grained quartz-ankerite-pyrite veins are zebra-striated in carbonaceous altered rocks
4	D29-1	960 m elevation, south flank of the No.2 ore body	I	Vein type ore	Quartz-dolomite-sphalerite-pyrite-galena veins developed in carbonaceous limestone
5	D45	960 m elevation, south flank of the No.2 ore body	I	Massive, brecciated ore	Medium-coarse-grained massive sphalerite-pyrite-dolomite aggregate, locally cementing breccias of carbonaceous altered rock
6	D48	860 m elevation, saddle part of the No.2 ore body	I	Disseminated ore	Fine-grained sphalerite, galena, pyrite, and dolomite are densely disseminated in altered rocks
7	DTZ-2-2	1060 m elevation, saddle part of the No.2 ore body	I	Mineralized carbonaceous limestone	Quartz-calcite veins are interspersed with carbonaceous limestone, with black aphanitic sphalerite developed at the edges
8	DTZ-1	1060 m elevation, south flank of the No.2 ore body	I	Mineralized carbonaceous phyllite	The carbonaceous phyllite contains lumpy, disseminated sphalerite, galena, and pyrite
9	DTZ-3-4	1060 m elevation, north flank of the No.2 ore body	I	Massive ore	Fine-grained black-brown lumpy sphalerite, with less quartz, pyrite, and galena
10	D41	860 m elevation, south flank of the No.2 ore body	I	Disseminated ore	Fine-grained sphalerite and ankerite are densely disseminated in grayish-black carbonaceous altered rocks
11	D213.2	960 m elevation, north flank of the No.2 ore body	I	Mineralized siliceous rock	Gray-black siliceous rock with disseminated fine-grained pyrite
12	D51-1	795 m elevation, south flank of the No.2 ore body	I	Disseminated ore	Fine-grained sphalerite, galena, pyrite, and dolomite are densely disseminated in altered rocks
13	D61-1	910 m elevation, saddle part of the No.2 ore body	I	Disseminated ore	Medium-fine-grained dense disseminated sphalerite, pyrite, and arsenopyrite are developed in silicified carbonaceous limestone
14	D229-1	960 m elevation, south flank of the No.2 ore body	I	Banded ore	Banded ankerite-sphalerite-pyrite-galena veins developed in altered carbonaceous limestone
15	D36	910 m elevation, south flank of the No.2 ore body		Granite porphyry dike	NWW-trending granite porphyry dike, nearly parallel to the ore body, with scattered pyrite
16	D55	960 m elevation, south flank of the No.1 ore body	II	Disseminated ore	Quartz-dolomite stockwork developed in the limestone, with fine-grained arsenopyrite and pyrite aggregate developed at the contact area

Table 1. Cont.

No.	Sample	Position	Stage	Type	Description
17	D58	960 m elevation, south flank of the No.1 ore body	II	Disseminated ore	Silicified limestone with disseminated pyrite, interspersed by quartz–dolomite stockwork
18	D107-3	795 m elevation, south flank of the No.2 ore body	II	Massive ore	The massive medium-fine-grained pyrite–sphalerite–arsenopyrite–ankerite aggregates, interspersed by the Stage III coarse-grained calcite and galena veins
19	D109	795 m elevation, south flank of the No.2 ore body	II	Massive ore	Pyrite-rich massive ore, micro-fine grained pyrite aggregates, cementing carbonaceous altered breccia
20	D205.2	795 m elevation, south flank of the No.2 ore body	II	Vein type ore	Veinlets composed of quartz, calcite, pyrite, sphalerite, and galena, crosscutting the altered rocks
21	D26	960 m elevation, saddle part of the No.2 ore body	III	Vein type ore	The medium-fine-grained lumpy sphalerite, galena, and calcite vein developed in the altered carbonatite
22	D230	960 m elevation, south flank of the No.2 ore body	III	Disseminated ore	Veinlet-disseminated ore, mineralized siliceous rock crosscutting by quartz–calcite–pyrite veins
23	D37-2	910 m elevation, north flank of the No.1 ore body	III	Gold bearing ore	The altered marl, with disseminated pyrite, interspersed with quartz–dolomite–pyrite vein
24	D223.3	795 m elevation, south flank of the No.2 ore body	III	Gold bearing ore	Dense disseminated pyrite is developed in the altered rock, with quartz–calcite aggregates

#### 4.1. CL and SEM

Thin sections of samples collected from different mining levels, representing different stages of mineralization, were selected for cathodoluminescence (CL) and scanning electron microscopy (SEM) imaging. CL investigation was carried out at State Key Laboratory of Geological Processes and Mineral Resources, China University of Geosciences, using an FEI Quanta 600 (MLA) with EDX and Gatan CL detectors (Gatan, Inc., Warrendale, PA, USA). SEM investigation was carried out at the Institute of Geology, Chinese Academy of Geological Sciences, using a FEI NOVA nanoSEM (Thermo Fisher Scientific, Brno, Czech Republic) equipped with an Oxford X-Max 50 detector (Oxford Instruments, Oxford, UK).

#### 4.2. In Situ S Isotope Analysis

Representative sphalerite, pyrite, and galena crystals of hydrothermal stage I to stage III, pyrite of sedimentary period, and pyrite of granite porphyry dike were selected for in situ LA-MC-ICP-MS sulfur isotope analysis by using a Resonetics-S155 excimer ArF laser ablation system with the Nu Plasma II multicollector ICP-MS (produced by Australian Scientific Instrument, Australia) at the State Key Laboratory of Geological Processes and Mineral Resources, China University of Geosciences, Wuhan. Detailed test methods followed Fu et al. (2016) and Zhu et al. (2016, 2017) [29–31]. The energy fluence of the laser was approximately 3 J/cm<sup>2</sup>. For single spot analysis, the diameter was 33 μm with a laser repetition rate of 8 Hz. The true sulfur isotope ratio was calculated by correction for instrumental mass bias by linear interpolation between the biases calculated from two neighboring standard analyses. Isotope data are reported in delta notation (‰) in comparison with Vienna Cañon Diablo Troilite (V-CDT):

$$\delta^{34}\text{S}_{\text{V-CDT}} = [((^{34}\text{S}/^{32}\text{S})_{\text{sample}} / (^{34}\text{S}/^{32}\text{S})_{\text{V-CDT}}) - 1] \times 10^3$$

where ( $^{34}\text{S}/^{32}\text{S}$ ) sample is the measured  $^{34}\text{S}/^{32}\text{S}$  ratio in the sample and ( $^{34}\text{S}/^{32}\text{S}$ )<sub>V-CDT</sub> is defined as 0.044163 [32]. The precision of  $^{34}\text{S}/^{32}\text{S}$  analysis is less than 0.00003 (1 $\sigma$ ). An in-house pyrite standard named WS-1 was used to calibrate the mass bias for S isotopes [30]. This consists of a natural pyrite crystal from the Wenshan polymetallic skarn deposit, Yunnan Province, China. The  $^{34}\text{S}_{\text{V-CDT}}$  value ( $0.3 \pm 0.1\%$ ) for WS-1 natural pyrite was determined using the CF-IRMS method on a MAT 253 isotope ratio mass spectrometer (Thermo Finnigan, Bremen, Germany) at the Institute of Mineral Resources, Chinese Academy of Geological Sciences, Beijing. Standards were measured before and after every four spot analyses. We also use the pyrite standard to obtain the data of galena and sphalerite, and these data should be considered as rough results due to no proper standard.

#### 4.3. In Situ Pb Isotope Analysis

Twenty-six analysis spots, including pyrite, galena, and sphalerite of hydrothermal stages I–III and pyrite of the granite porphyry dike, were selected for in situ LA-MC-ICP-MS lead isotope analysis. The examination was conducted utilizing a 193 nm laser ablation system (RESOLUTION M-50, ASI) interfaced with a Nu Plasma II multicollector ICP-MS (Wrexham, UK) at the State Key Laboratory of Continental Dynamics, Department of Geology, Northwest University, Xi'an. Homogeneous nano-particulate pressed sulfide powder tablets (PSPTs) served as reference materials to ensure measurement accuracy. Instrument parameters were optimized using the NIST610 standard (Pb = 426  $\mu\text{g/g}$ ) [33] to achieve maximal analytical sensitivity, signal stability, and optimal peak shape and alignment. Analytical signals were deduced using the Time Resolved Analysis (TRA) mode, with an integration time of 0.2 s. Each measurement spot encompassed a 30 s background measurement, followed by 50 s of ablation for signal collection, and an additional 120 s for wash time to mitigate memory effects. Galena laser ablation operated at a frequency of 2 Hz with a spot size of 9  $\mu\text{m}$ , while for bismuthinite, the frequency was 6 Hz with a spot size of 30  $\mu\text{m}$ , respectively. The  $^{202}\text{Hg}$ ,  $^{203}\text{Tl}$ ,  $^{204}\text{Hg}+^{204}\text{Pb}$ ,  $^{205}\text{Tl}$ ,  $^{206}\text{Pb}$ ,  $^{207}\text{Pb}$ , and  $^{208}\text{Pb}$  ion beams were collected by corresponding Faraday cups. The  $^{204}\text{Hg}/^{202}\text{Hg}$  natural abundance ratio (0.229883) was used to calculate and determine the interference from the  $^{204}\text{Hg}$  species on the  $^{204}\text{Pb}$  intensity obtained. Analytical procedures, reference material PSPTs, and data processing have been previously described in detail by Chen et al. (2014), Yuan et al. (2015), and Bao et al. (2017) [33–35].

#### 4.4. Rb–Sr Isotope Analyses

The sulfide samples of Stage I were rinsed several times in distilled water, dried, and crushed to 40–60-mesh size. The individual minerals of sphalerite and pyrite were handpicked under a binocular microscope, with purity levels of >98% being used for analysis. Sulfide grains were crushed to <200 mesh using an agate ball mill, then washed in an ultrasonic bath and dried. For Rb–Sr isotope analyses, powder weighing 0.2–0.3 g of each sample were dissolved in Teflon beakers with a mix of HF and HNO<sub>3</sub> acids. Rb–Sr have been separated for isotopic analysis by adopting the resin of AG50W $\times$ 8 and different eluent reagents. Firstly, REEs are separated from Rb–Sr by using the normal method of cation–exchange chromatography with eluent of HCl. Then, Rb and Sr were separated using a cation–ion exchange column.

Sulfide samples underwent Rb–Sr isotopic analyses using a VG 354 mass spectrometer (VG Instruments Group Limited from UK) equipped with five collectors at the Center of Modern Analysis, Nanjing University. The chemical separation and mass spectrometric procedures are outlined by Wang et al. (2006) [36].  $^{87}\text{Sr}/^{86}\text{Sr}$  is normalized to  $^{86}\text{Sr}/^{88}\text{Sr} = 0.1194$ , to correct for instrumental fractionation. During the period of this study, measurements for the American Standard Reference Material NBS 987 Sr standard gave  $^{87}\text{Sr}/^{86}\text{Sr} = 0.710236 \pm 0.000007$  (2 $\sigma$ ).

#### 4.5. Sm–Nd Isotope Analyses

The carbonate minerals of ankerite, dolomite, and calcite in the Dongtangzi Zn–Pb deposit were systematically collected from hydrothermal mineralization period sphalerite–galena–pyrite–quartz–ankerite–dolomite–calcite veins within the main orebody, with six samples from Stage I, two from Stage II, and one from Stage III, respectively. These carbonate minerals were separated from the ore samples after crushing and were powdered in an agate mill before Sm–Nd isotopic analysis.

Powders of carbonate mineral specimens underwent dissolution utilizing purified 0.5 M dilute acetic acid at an ambient temperature over a four-hour duration. After centrifugation, acid-insoluble residues underwent digestion employing a mixture of HNO<sub>3</sub>, HF, and HClO<sub>4</sub>, rendering them amenable for Nd isotopic analyses. The Nd solutions were subjected to separation through conventional ion exchange techniques. The isotopic compositions of the refined Nd solutions were quantified utilizing a VG 354 mass spectrometer equipped with five collectors at the Center of Modern Analysis, Nanjing University. A comprehensive account of the experimental methodology can be found in the reports by Wang Y.X. et al. (2007) [37].

## 5. Results

### 5.1. In Situ S Isotopic Compositions

A total of 50 spots were assessed for the in situ sulfur isotope study, covering pyrite from the sedimentary period (n = 4); sulfides from the hydrothermal period in Stage I (n = 23), Stage II (n = 4), and Stage III (n = 15), and pyrite in the granite porphyry dike (n = 4). The results are listed in Table 2.

**Table 2.** In situ S isotopic composition of the sulfides from the Dongtangzi Zn–Pb deposit.

Sample/Point No.	Stage	Mineral	$\delta^{34}\text{S}$ (‰)
D216.3/1	Sedimentary period	Pyrite	16.9
D216.3/2		Pyrite	15.8
D216.3/5		Pyrite	19.9
D216.3/6		Pyrite	21.4
D216.3/3	Hydrothermal I	Sphalerite	7.3
D216.3/4		Sphalerite	8.7
D41/1		Sphalerite	9.1
D41/2		Pyrite	8.6
D41/3		Sphalerite	9.3
D41/4		Sphalerite	9.4
D41/5		Sphalerite	8.8
D51/1		Pyrite	8
D51/2		Galena	2.7
D51/3		Sphalerite	7.3
D51/4		Sphalerite	7
D51/5		Sphalerite	8
D51/6		Galena	1.4
D51/7		Galena	2.7
D51/8		Pyrite	7.1
D51/9		Sphalerite	7.1
D61/1		Pyrite	5.3
D61/2		Sphalerite	8.6
D61/3		Galena	1.1
D61/4		Sphalerite	8.8
D61/5		Sphalerite	8.9
D213.2/1		Sphalerite	8.3
D213.2/2		Sphalerite	8.8

Table 2. Cont.

Sample/Point No.	Stage	Mineral	$\delta^{34}\text{S}$ (‰)
D36.1/1	Granite porphyry dike	Pyrite	2.1
D36.1/2		Pyrite	4.3
D36.1/3		Pyrite	3.7
D36.1/4		Pyrite	2.5
D205.2/1	Hydrothermal II	Pyrite	7.4
D205.2/2		Chalcopyrite	6.4
D205.2/3		Pyrite	7.3
D205.2/4		Chalcopyrite	6.5
D26/1	Hydrothermal III	Sphalerite	9.9
D26/2		Galena	4.4
D26/3		Sphalerite	9.5
D26/4		Galena	4.8
D26/5		Sphalerite	9.9
D26/6		Pyrite	10.2
D26/7		Sphalerite	9.3
D26/8		Galena	4.6
D223.3/1		Pyrite	8.9
D223.3/2		Pyrite	3.8
D223.3/3		Pyrite	5
D223.3/4		Pyrite	4.4
D223.3/5		Pyrite	8.7
D223.3/6		Pyrite	7.2
D223.3/7		Pyrite	8.3

The measured  $\delta^{34}\text{S}$  data of pyrite from the sedimentary period and the granite porphyry dike vary from 15.8 to 21.4‰ (averaging 18.5‰), and from 2.1 to 4.3‰ (averaging 3.2‰), respectively. On the other hand, those of the sulfides from the three hydrothermal mineralization stages vary from 1.1 to 9.4‰ (averaging 7.1‰), from 6.4 to 7.4‰ (averaging 6.9‰), and from 3.8 to 10.2‰ (averaging 7.3‰), respectively, showing a relatively restricted range, indicating that there are no significant differences in the source of the sulfur during the hydrothermal mineralization stages.

### 5.2. In Situ Pb Isotopic Compositions

All the sulfides analyzed have similar lead isotope values and the radioactive lead content is low (Table 3). The  $^{206}\text{Pb}/^{204}\text{Pb}$ ,  $^{207}\text{Pb}/^{204}\text{Pb}$ , and  $^{208}\text{Pb}/^{204}\text{Pb}$  ratios in Stage I are 18.074–18.107, 15.641–15.663, and 38.217–38.764, respectively. Those in Stage II are 18.073–18.082, 15.652–15.659, and 38.301–38.324, respectively. For the Stage III, the ratios are 18.078–18.265, 15.645–15.654, and 38.293–38.310, respectively. For the granite porphyry dike, the ratios are 18.091–18.101, 15.585–15.610, and 38.169–38.241, respectively.

Table 3. In situ Pb isotopic composition of the sulfides from the Dongtangzi Zn-Pb deposit.

Sample/Point No.	Stage	Mineral	$^{208}\text{Pb}/^{204}\text{Pb}$	$^{207}\text{Pb}/^{204}\text{Pb}$	$^{206}\text{Pb}/^{204}\text{Pb}$
D36/1	Granite porphyry dike	Pyrite	$38.189 \pm 0.010$	$15.595 \pm 0.004$	$18.091 \pm 0.011$
D36/2		Pyrite	$38.241 \pm 0.009$	$15.61 \pm 0.004$	$18.101 \pm 0.003$
D36/3		Pyrite	$38.169 \pm 0.005$	$15.585 \pm 0.002$	$18.092 \pm 0.002$
D51/2	Hydrothermal I	Pyrite	$38.448 \pm 0.005$	$15.663 \pm 0.002$	$18.076 \pm 0.003$
D51/3		Pyrite	$38.286 \pm 0.004$	$15.652 \pm 0.001$	$18.078 \pm 0.002$
D51/4		Pyrite	$38.324 \pm 0.004$	$15.65 \pm 0.002$	$18.074 \pm 0.002$
D51/1		Sphalerite	$38.764 \pm 0.026$	$15.662 \pm 0.005$	$18.075 \pm 0.001$
D51/1		Galena	$38.336 \pm 0.008$	$15.661 \pm 0.003$	$18.084 \pm 0.001$

Table 3. Cont.

Sample/Point No.	Stage	Mineral	$^{208}\text{Pb}/^{204}\text{Pb}$	$^{207}\text{Pb}/^{204}\text{Pb}$	$^{206}\text{Pb}/^{204}\text{Pb}$
D51/2		Galena	$38.319 \pm 0.007$	$15.654 \pm 0.003$	$18.105 \pm 0.002$
D51/3		Galena	$38.234 \pm 0.006$	$15.647 \pm 0.002$	$18.096 \pm 0.002$
D51/4		Galena	$38.234 \pm 0.009$	$15.646 \pm 0.003$	$18.086 \pm 0.002$
D61/1		Galena	$38.217 \pm 0.004$	$15.643 \pm 0.002$	$18.107 \pm 0.005$
D61/2		Galena	$38.222 \pm 0.007$	$15.642 \pm 0.002$	$18.102 \pm 0.003$
D61/3		Galena	$38.218 \pm 0.005$	$15.641 \pm 0.002$	$18.096 \pm 0.002$
D61/4		Galena	$38.293 \pm 0.001$	$15.647 \pm 0.001$	$18.087 \pm 0.002$
D61/5		Galena	$38.291 \pm 0.004$	$15.645 \pm 0.001$	$18.090 \pm 0.003$
D205-2/1	Hydrothermal II	Pyrite	$38.307 \pm 0.024$	$15.652 \pm 0.009$	$18.074 \pm 0.002$
D205-2/2		Pyrite	$38.324 \pm 0.006$	$15.659 \pm 0.002$	$18.074 \pm 0.002$
D205-2/3		Pyrite	$38.314 \pm 0.005$	$15.655 \pm 0.002$	$18.073 \pm 0.002$
D205-2/4		Pyrite	$38.321 \pm 0.005$	$15.659 \pm 0.002$	$18.082 \pm 0.001$
D205-2/5		Pyrite	$38.301 \pm 0.007$	$15.65 \pm 0.003$	$18.080 \pm 0.001$
D26/1	Hydrothermal III	Galena	$38.301 \pm 0.007$	$15.646 \pm 0.003$	$18.097 \pm 0.002$
D26/2		Galena	$38.306 \pm 0.005$	$15.649 \pm 0.024$	$18.086 \pm 0.003$
D26/3		Galena	$38.299 \pm 0.006$	$15.646 \pm 0.002$	$18.091 \pm 0.004$
D26/4		Galena	$38.293 \pm 0.003$	$15.645 \pm 0.001$	$18.265 \pm 0.005$
D26/5		Galena	$38.310 \pm 0.003$	$15.654 \pm 0.001$	$18.078 \pm 0.002$

### 5.3. Rb–Sr Isochron Age

The analytical data are listed in Table 4. The Rb contents of the samples are low, ranging from  $0.235 \times 10^{-6}$  to  $1.207 \times 10^{-6}$ , and the Sr contents are also low, ranging from  $0.3105 \times 10^{-6}$  to  $5.218 \times 10^{-6}$ . The  $^{87}\text{Rb}/^{86}\text{Sr}$  values range from 0.528 to 6.971. The  $^{87}\text{Sr}/^{86}\text{Sr}$  values have a wide range, from 0.71204 to 0.73148. Regression and age calculations of isochrons were performed using Isoplot/Ex Version 3.00 software [38] and with  $\lambda = 1.42 \times 10^{-11} \text{ a}^{-1}$ , using 1% errors for  $^{87}\text{Rb}/^{86}\text{Sr}$  ratios and 0.05% errors for  $^{87}\text{Sr}/^{86}\text{Sr}$  ratios at a confidence level of 95%. The analytical data yielded an isochron age of  $211.6 \pm 2.6 \text{ Ma}$  for mineralization in Stage I, with an initial  $^{87}\text{Sr}/^{86}\text{Sr}$  ratio of  $0.71046 \pm 0.00012$  and an MSWD value of 0.31 (Figure 9a).

Table 4. Analytical data of Rb–Sr isotope ratios and Rb–Sr contents.

Sample No.	Mineral	Stage	Rb ( $\mu\text{g/g}$ )	Sr ( $\mu\text{g/g}$ )	$^{87}\text{Rb}/^{86}\text{Sr}$	$^{87}\text{Sr}/^{86}\text{Sr}$	$2\sigma$
DTZ-2-2	Spalerite	I	0.4932	2.7590	0.5278	0.712041	0.000008
DTZ-1	Pyrite	I	1.2070	5.2180	0.6794	0.712506	0.000008
DTZ-1	Galena	I	0.2347	0.3742	1.8150	0.715902	0.000009
DTZ-1	Spalerite	I	0.7834	1.6930	1.3620	0.714581	0.000010
DTZ-3-4	Galena	I	0.3728	0.3105	3.5470	0.721159	0.000008
DTZ-3-4	Spalerite	I	0.9346	0.3957	6.9710	0.731475	0.000009

Considering the potential for physical deformation of the ore, there exists a plausible scenario in which the determined ages might be influenced by tectonic overprint, necessitating further investigation of this aspect. The assessment of  $1/\text{Rb}$  versus  $^{87}\text{Rb}/^{86}\text{Sr}$  diagrams provides a way through which discern whether the initial  $(^{87}\text{Sr}/^{86}\text{Sr})_i$  values remained constant throughout the sulfide growth process [39], thereby enabling an evaluation of data integrity. In the present investigation, the absence of covariation between  $1/\text{Rb}$  values and  $^{87}\text{Rb}/^{86}\text{Sr}$  (Figure 9b) signifies that the isochron age data are meaningful, offering a reliable age of the ore formation.

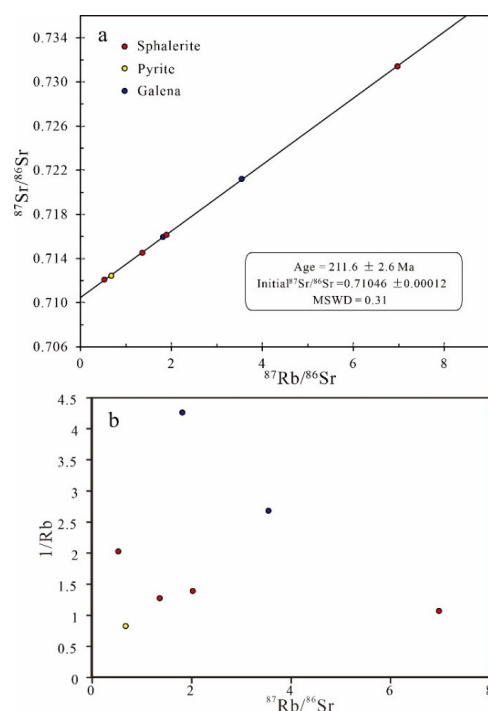


**Figure 9.** (a) Rb–Sr isochron age of sulfides from the Dongtangzi Zn-Pb deposit; (b) Diagram of  $1/\text{Rb}$  versus  $^{87}\text{Rb}/^{86}\text{Sr}$ .

#### 5.4. Sm-Nd Isochron Age

All  $^{143}\text{Nd}/^{144}\text{Nd}$  ratios determined for the ankerite, dolomite, and calcite samples of the hydrothermal mineralization stages analyzed during this study were normalized to  $^{146}\text{Nd}/^{144}\text{Nd} = 0.7219$ , with results and analytical uncertainties ( $2\sigma$ ) given in Table 5. The  $^{147}\text{Sm}/^{144}\text{Nd}$  values for carbonate minerals from Stage I range from 0.0731 to 0.7195, with corresponding  $^{143}\text{Nd}/^{144}\text{Nd}$  values ranging from 0.511851 and 0.512739.

**Table 5.** The Sm-Nd isotopic data of the stage I carbonates from the Dongtangzi Zn-Pb deposit.

Sample No.	Mineral	Stage	Sm ( $\times 10^{-6}$ )	Nd ( $\times 10^{-6}$ )	$^{147}\text{Sm}/^{144}\text{Nd}$	$^{143}\text{Nd}/^{144}\text{Nd}$
D22	Dolomite	I	0.1605	3.527	0.1351	$0.511943 \pm 9$
D28-4	Ankerite	I	0.6537	2.678	0.7195	$0.512739 \pm 7$
D29-1	Dolomite	I	0.4058	4.634	0.2586	$0.512081 \pm 8$
D45-31	Dolomite	I	0.1325	5.336	0.0731	$0.511851 \pm 8$
D45-32	Dolomite	I	0.3536	5.781	0.1803	$0.511982 \pm 7$
D48	Dolomite	I	0.2953	4.013	0.2175	$0.512024 \pm 9$
D55	Dolomite	II	0.4831	3.907	0.3656	$0.512229 \pm 14$
D58	Calcite	II	0.5029	2.694	0.5498	$0.512501 \pm 8$
D58	Dolomite	II	0.1847	5.325	0.1023	$0.511875 \pm 9$

Regression and age calculations of isochrons were performed using Isoplot/Ex Version 3.00 software [38]. The ratio errors of  $^{147}\text{Sm}/^{144}\text{Nd}$  and  $^{143}\text{Nd}/^{144}\text{Nd}$  were 1% and 0.03%, respectively. The carbonate minerals yielded an isochron age of  $211 \pm 4$  Ma (Figure 10a), with a mean square of weighted deviate (MSWD) value of 7.3 and an initial  $^{143}\text{Nd}/^{144}\text{Nd}$  ratio of  $0.511731 \pm 0.000009$  (Figure 10a). The nonlinear relationship between the plots on the  $1/\text{Nd}$  vs.  $^{143}\text{Nd}/^{144}\text{Nd}$  diagram (Figure 10b) excludes the possibility of a mixing line. Thus, the Sm-Nd isochron age may represent the mineralization age.

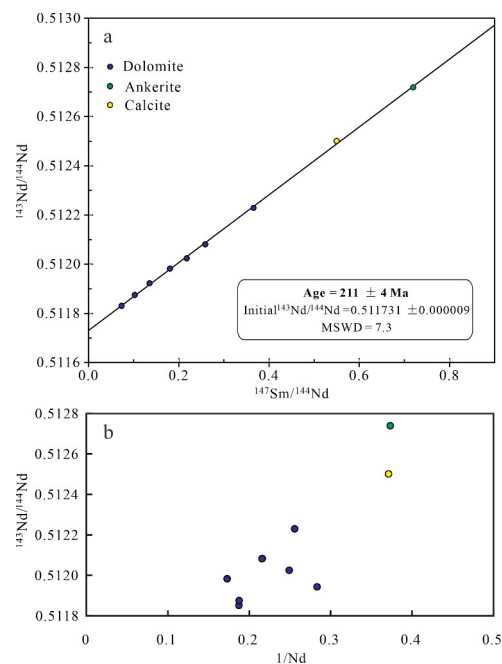


**Figure 10.** (a) Sm-Nd isochron age diagram of carbonates from the Dongtangzi Zn-Pb deposit; (b) Diagram of  $1/\text{Nd}$  vs.  $^{143}\text{Nd}/^{144}\text{Nd}$ .

## 6. Discussion

### 6.1. Sources of Sulfur and Metals

#### 6.1.1. Source of Sulfur

The sulfur isotopic compositions of sulfides extracted from mineral deposits traditionally serve as discerning indicators of sulfur sources, offering insights into ore formation conditions and genesis. Alterations in  $\delta^{34}\text{S}$  values are commonly associated with shifts in source, temperature, pH, and oxygen fugacity ( $f\text{O}_2$ ) [40–42]. The array of  $\delta^{34}\text{S}$  values within a specific region furnishes valuable information regarding the dynamics of sulfide precipitation, sulfate reduction processes, and the extent of isotopic fractionation, as well as discerning whether the fluid system was open or closed, contingent on a limited or unlimited sulfate supply [41,43,44].

Many views about the sulfur source of Zn-Pb deposits in the Fengtai ore cluster have been proposed, such as (1) a mixed source of reduced sulfur in seawater sulfate and sulfur in deep-sea hydrothermal fluids, via the decomposition of metal sulfide complexes in hydrothermal fluids or a combination of metal chloride complexes in hydrothermal fluids with basinal  $\text{H}_2\text{S}$  [45]; (2) a mixture of  $^{32}\text{S}$ -concentrated sulfur formed via a biological reduction with sulfur extracted from the sulfate and sulfide in the sedimentary formation [5]; and (3) seawater sulfate mixed with sulfur that leached from the basement rock [46]. However, previous works have not separately studied different sulfides from different mineralization stages, and no in situ analysis has been conducted, meaning that the mixing of sulfides from different stages and sources has been unavoidable.

Using the most advanced in situ LA-ICP-MS analysis method, in this work, sulfur isotopic compositions of sulfides from different episodes were obtained. Pyrite from the sedimentary period is  $^{34}\text{S}$  enriched ( $\delta^{34}\text{S}$  15.8‰~21.4‰), which is identical to the seawater sulfate from the Middle Devonian period [47]. The sulfides from the hydrothermal mineralization period have  $\delta^{34}\text{S}$  values ranging from 1.1‰ to 10.2‰, with peak values ranging from 6‰ to 10‰ (Figure 11), partly overlapping that of the granite porphyry dike pyrite (2.1‰~4.3‰) (Table 2, Figure 11). The  $\delta^{34}\text{S}$  values obtained in this work can be divided into two main end members: magmatic source (2.1 to 4.3‰) and seawater sulfate source (15.8 to 21.4‰). Moreover, the  $\delta^{34}\text{S}$  values of the ore sulfides are between the two end members (1.1‰~10.2‰), indicating a mixed source of magmatic sulfur and seawater

sulfate. Wilkinson and Hitzman (2014) [48] put forward the hypothesis that magmatic heat, originating from the sub-crustal emplacement of mid-crustal sills, may serve as a catalyst for the regional fluid flow associated with Irish-type deposits. Similarly, Slack et al. (2015) [49] demonstrated that the ore-forming fluid of the black shale-hosted Red Dog Zn-Pb-Ag deposit emanated from hydrothermal fluids that leached from mafic and ultramafic rocks at depth. Therefore, contemporaneous magmatic activities at depth could have functioned as a primary or partial source of sulfur in carbonate-hosted Pb-Zn deposits, including the Dongtangzi Zn-Pb deposit.

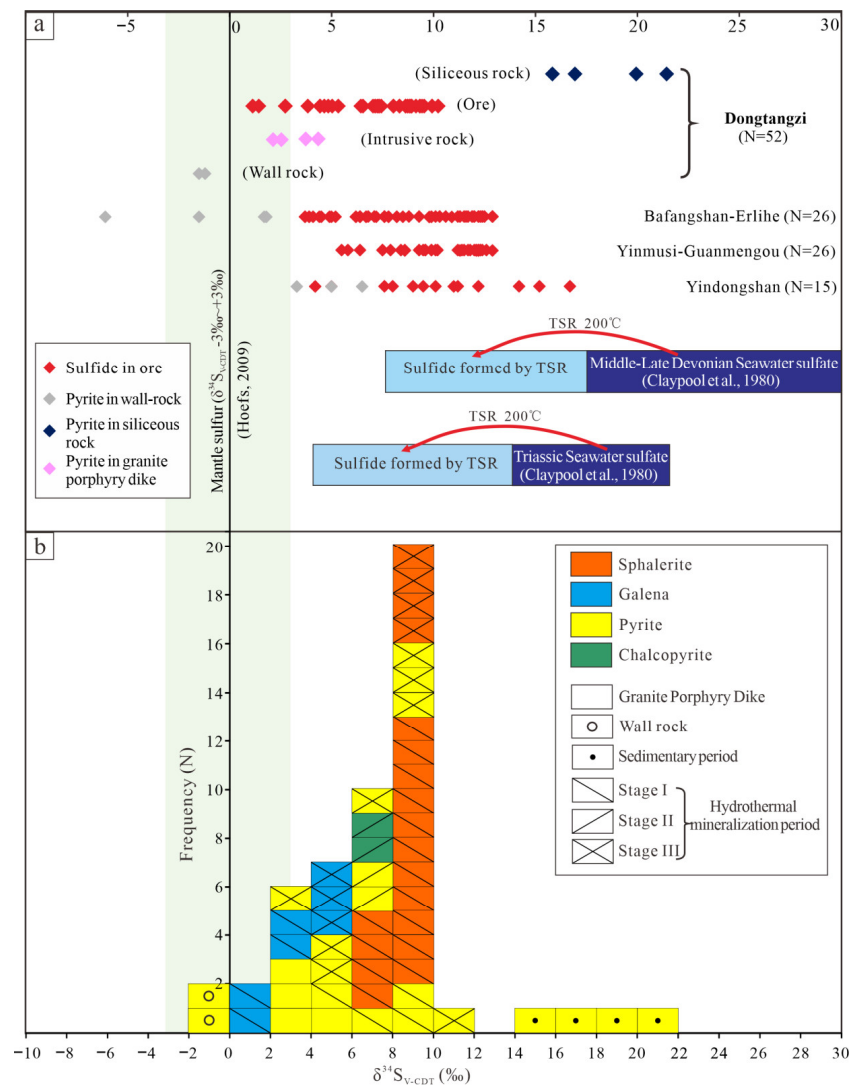


**Figure 11.** (a) Comparison diagram of sulfur isotope of the Pb-Zn deposits in the Fengtai ore cluster and (b) sulfur isotopic composition histogram of sulfides of the Dongtangzi Zn-Pb deposit. Note: The data of pyrite in the wall rock of the Dongtangzi deposit (gray dots) are from Wang J.L. et al. (1996) [5], and the others are obtained from this work. The data of the Bafangshan–Erlihe, Yinmushi–Guanmengou and Yindongshan deposits are from Hu Q.Q. (2015a) [21], and the data of the Middle–Late Devonian and Triassic Marine sulfate are from Claypool et al. (1980) [49].

Compared with pyrite from the hydrothermal mineralization period (averaging 7.2‰), pyrite from the sedimentary period is remarkably rich in heavy sulfur (averaging 18.5‰), showing a seawater sulfate source, while the values of pyrite in the granite porphyry dike (averaging 3.2‰) are closer to those of mantle-derived sulfur. The veined Stage I sphalerite in the siliceous rock ranges from 7.3 to 8.7‰ (sample D216.3), while the syngenetic

disseminated pyrites from the siliceous rock are the richest in heavy sulfur, ranging from 15.8 to 21.4‰ (sample D216.3), indicating that the sulfides from different stages had not reached isotopic equilibrium, even being hosted in the same thin section. In general, if  $\delta^{34}\text{S}_{\text{pyrite}} > \delta^{34}\text{S}_{\text{sphalerite}} > \delta^{34}\text{S}_{\text{galena}}$ , then the fractionation of S isotopes among minerals reached equilibrium [50]. The  $\delta^{34}\text{S}$  values of the sulfides from the hydrothermal mineralization period show  $\delta^{34}\text{S}_{\text{sphalerite}} > \delta^{34}\text{S}_{\text{pyrite}} > \delta^{34}\text{S}_{\text{galena}}$  (Table 2, mineral pairs from samples D51, D61, and D26), demonstrating that sphalerite and galena have reached equilibrium, but pyrite and sphalerite have not. This disequilibrium between pyrite and sphalerite could be explained by the mixing of magmatic sulfur during hydrothermal crystallization.

Wang X. et al. (1996) [19] obtained a range of 165–320 °C for the homogenization temperature of the fluid inclusions in quartz and sphalerite from the main mineralization stage of the Dongtangzi Zn-Pb deposit. Usually, the thermochemical sulfate reduction (TSR) reaction that occurs at around 200 °C will cause about 10‰ sulfur isotope fractionation between sulfates and reduced sulfurs [51,52]. As the temperature increases, the degree of sulfur isotope fractionation caused by the TSR reaction gradually decreases, and there is generally no obvious sulfur isotope fractionation between sulfide minerals and reduced sulfur during mineral precipitation [53]. Holser and Kaplan (1966) [54] first proposed that the  $\delta^{34}\text{S}$  values of seawater reached a minimum in the Middle Devonian period and then rapidly reached a maximum in the late Devonian period (about 17‰ in the Middle Devonian VS. about 30‰ in the Late Devonian period). The rapid increase in global seawater sulfur isotope values during the Devonian and Early Triassic periods was possibly due to the rapid precipitation of pure sulfide minerals [47].

If the sulfur in the Pb-Zn sulfides of the Dongtangzi deposit mainly comes from Devonian seawater sulfate, then the  $\delta^{34}\text{S}$  values of sulfides formed by the seawater sulfate TSR reaction at around 200 °C would be around 12‰ (the light blue area in Figure 11a), which is obviously higher than the measured  $\delta^{34}\text{S}$  values (1.1‰~10.2‰, Figure 11a,b). A single TSR process in Devonian seawater sulfate would not result in such a low sulfur isotopic composition; hence, a great deal of light sulfur must have been involved during the mineralization processes. Possible sources include the following: (1) magmatic sulfur since some of the Pb-Zn sulfides have consistent sulfur isotope compositions, with pyrite in the granite porphyry dike (2.1 to 4.3‰, Figure 11), as obtained in this study; (2) sulfides enriched in light sulfur isotopes through a biogeochemical reduction reaction (BSR) in the seawater sulfate during sedimentation, which is supported by the light sulfur isotope enriched pyrite ( $\delta^{34}\text{S} < 0$ ‰) found in the wall rock of the Dongtangzi deposit (−1.5~−1.1‰, Figure 11a); and (3) the seawater sulfate of the Triassic sedimentary basin distributed to the south of the Fengtai ore cluster, because Triassic seawater sulfate is relatively enriched in light sulfur isotopes, which could potentially generate sulfides via TSR (around 8‰; the light blue area in Figure 11a) with similar  $\delta^{34}\text{S}$  ranges to the Pb-Zn sulfides in the Dongtangzi deposit (1.1‰~10.2‰, Figure 11a). During the Middle Triassic period, the west Qinling orogenic belt experienced a rapid transformation from Yangtze-type stable shallow carbonate sedimentation to Tethys-type deep-sea thick turbidite sedimentation. The Tethys-type rift basin opened in the Middle Triassic period, and rapidly closed between the Middle Triassic and early Late Triassic period, developing complexly folded deformation in the rigid massif, sandwiched between the two ancient blocks [55]. This rapid basin closure during Triassic is conducive to the deposition of evaporites, and the subsequent folding deformation provided the possibility of dissolution, infiltration, and long-distance transportation of these evaporites. To the southeast of the Fengtai ore cluster, abundant evaporites are developed in the sedimentary rocks of the Middle Triassic Jialingjiang Formation in the northern margin of the Yangtze Block, adjacent to the south Qinling belt, such as the Wadaozi, Huodigou, and Zuoxigou gypsum deposits [56,57].

In short, the sulfur associated with the Zn-Pb mineralization of the Dongtangzi deposit has a mixed source of magmatic sulfur and seawater sulfate of evaporites from regional sedimentary formation, precipitated by TSR.

### 6.1.2. Source of Lead

Given the markedly diminished concentrations of thorium (Th) and uranium (U) in sulfide minerals, particularly in galena, the accrued influence of U and Th on radiogenic lead (Pb) isotopes within sulfides is deemed negligible, as attested by previous studies [58–60]. Consequently, the lead isotopic ratios derived from galena, sphalerite, and pyrite in the Dongtangzi deposit could represent the isotopic composition of the associated hydrothermal fluids.

Earlier studies suggested that the metals of the Dongtangzi Zn-Pb deposit originated from host Devonian to Carboniferous carbonate rocks [19], and/or from deep magmatic hydrothermal fluid [11]. The lead isotopic composition of the major deposits in the Fengtai ore cluster (e.g., the Qiandongshan, the Yindongliang, the Bafangshan, and the Yinmusi) exhibit a relatively uniform and stable nature, with variations typically smaller than 1% [5]. These findings indicate the presence of stable and normal lead with a high  $\mu$ -value, suggesting a mixed source of lead originating from the crust within the orogenic belt. Qi et al. (1993) [15] further noted that the sulfur and lead in the lead–zinc deposits of the Fengtai ore cluster originated from two distinct source regions; that is, the sulfur was derived from sea water while the lead originated from the basement rock. Wang X. et al. (1996) [19] proposed that the primary Pb-Zn source of the Pb-Zn deposits in the Fengtai ore cluster was the high-uranium crust rather than the mantle. This ore displayed characteristics of mixed lead, while the source region exhibited typical features associated with orogenic belts. Wang J.L. et al. (1996) [5] further postulated that the initially enriched lead in the ancient strata within the source region underwent leaching by subterranean hot water and was subsequently transported along growth faults to the seafloor, where mineralization occurred. The anomalous lead observed in the ore was attributed to the incorporation of crustal lead during later modification processes [5]. However, prior investigations failed to differentiate sulfides from different mineralization stages and were not conducted in situ, resulting in the unavoidable mixing of lead from various stages and sources within the same sample.

In this study, the in situ Pb isotope compositions of sulfides from different mineralization stages in the Dongtangzi deposit demonstrate a consistent and stable lead isotope composition across different hydrothermal mineralization stages. The narrow range of the bulk isotopic data suggests a single source or else a well-mixed source of Pb (Table 3, Figure 12) [61]. However, the lead isotopic composition of the ore sulfides is different from that of pyrite found in the granite porphyry dikes (Figure 12), indicating that they may have different source regions. In other words, the ore sulfides are close to the upper crust, while the pyrite of the granite porphyry dikes are close to the orogenic belt (Figure 12a). This suggests that the primary origin of the lead–zinc elements may be from upper-crust sources rather than from magmatic sources. The lead isotope composition diagram illustrates that the ore sulfides of the Dongtangzi deposit and Triassic granitic rocks such as the Xiba intrusion in the west Qinling orogen (Figure 12) have similar lead isotope compositions, indicating that they may share the same source area. Meanwhile, the lead isotope compositions of the ore sulfides partially overlap with those of the Neoproterozoic Yaolinghe Group and Bikou Group metamorphic basement rocks (Figure 12) beneath the Fengtai ore cluster. Such Pb isotopic signatures rule out contributions of Pb from the Paleozoic Mianlue oceanic crust (Figure 12).

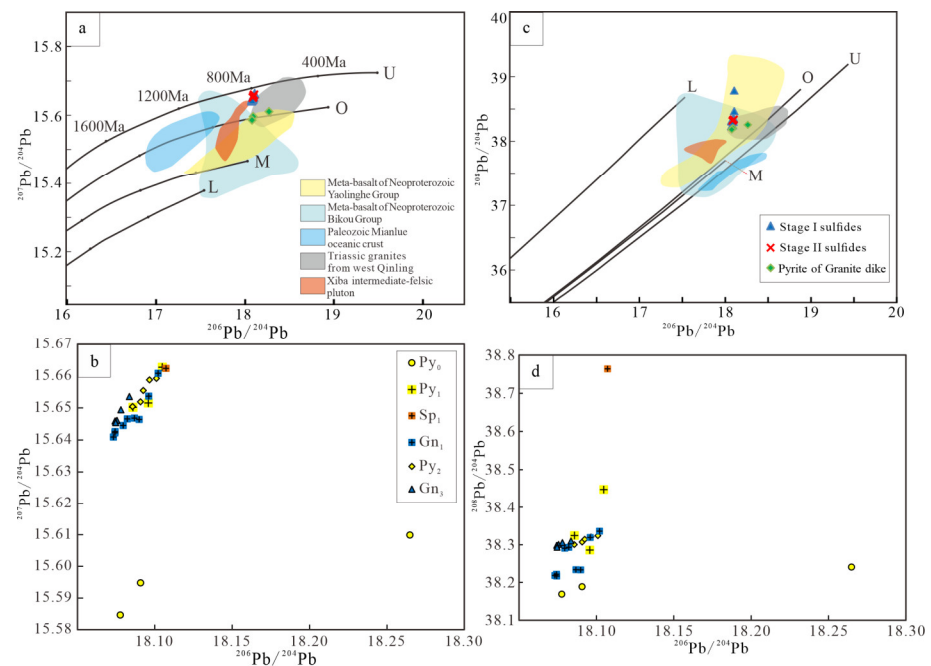


**Figure 12.** Comparison diagram of lead isotopes of the Dongtangzi Zn-Pb deposit. Plots of  $^{206}\text{Pb}/^{204}\text{Pb}$  vs.  $^{207}\text{Pb}/^{204}\text{Pb}$  (a,b) and  $^{206}\text{Pb}/^{204}\text{Pb}$  vs.  $^{208}\text{Pb}/^{204}\text{Pb}$  (c,d). Trends for the upper crust (U), orogenic belt (O), mantle (M), and lower crust (L) are taken from Zartman and Doe (1981) [62]. Data for the Triassic granites from west Qinling orogenic belt are from Zhang et al. (2006), Zhang et al. (2007a, b), Qin et al. (2007, 2008a, 2008b, 2010) [63–66]; the Neoproterozoic Yaolinghe and Bikou meta-volcanic rocks are from Xia et al. (2007, 2008) [67,68]; and the Paleozoic Mianlue oceanic crust are from Xu et al. (2002) [69]. Py<sub>0</sub>: pyrite of sedimentary period; Py<sub>1</sub>, Py<sub>2</sub>: pyrite of the Stage I and Stage II; Sp<sub>1</sub>: sphalerite of the Stage I; Gn<sub>1</sub>, Gn<sub>3</sub>: galena of the Stage III.

These findings suggest that the metallic materials involved in ore formation originate from a mixture of Triassic magmatic hydrothermal fluid and metamorphic basement. The remarkably homogeneous lead isotope composition of the ore sulfide (Table 3, Figure 12) mirrors that of global Mississippi Valley-type (MVT) or SEDEX-type Pb-Zn deposits [70,71], indicating the thorough mixing of ore-forming fluids within the source region.

## 6.2. Timing of the Ore Formation

The isotope dating of ore minerals is the best method through which to determine the age of a hydrothermal deposit. Obtaining the age of associated gangue minerals can further determine the metallogenic age. Since different mineral phases have different chemical potential, paragenetic minerals with different chemical properties precipitated from the same ore-forming fluid may have different Rb/Sr and Sm/Nd values. Consequently, for the dating of hydrothermal deposits, the hydrothermal mineral assemblage proves more advantageous than a single-mineral species [72]. The sulfide Rb–Sr isochron dating method has been widely used for dating Pb-Zn deposits [73–82]. Moreover, calcium-bearing minerals such as calcite and fluorite in hydrothermal deposits are ideal objects for Sm-Nd isotopic dating [83–88].

The temporal evolution within a hydrothermal deposit may span several million years, contrasting with a narrower timeframe of hundreds of thousands of years for a cohort of paragenetic hydrothermal minerals. Therefore, in the context of Rb–Sr or Sm-Nd isochron dating, the paragenetic minerals could be treated as having formed synchronously [72].

In order to eliminate submicroscopic fluid inclusions that might have contaminated the results, single sulfide mineral particles were ground to sizes below 200 mesh, followed by ultrasonic cleaning, effectively mitigating the interference from fluid inclusions within the minerals. Following the discriminant diagram proposed by Pettke et al. (1996) [89], the

constancy of the initial  $^{87}\text{Sr}/^{86}\text{Sr}$  values during sulfide mineral growth can be determined by utilizing a  $1/\text{Rb}-^{87}\text{Rb}/^{86}\text{Sr}$  relation diagram, thus assessing the validity of the data. The  $1/\text{Rb}-^{87}\text{Rb}/^{86}\text{Sr}$  relation diagram (Figure 9b) demonstrates that the data points do not exhibit linear correlation. The Rb and Sr contents vary across distinct single-mineral sphalerite, galena, and pyrite samples, while the  $^{87}\text{Sr}/^{86}\text{Sr}$  and  $^{87}\text{Rb}/^{86}\text{Sr}$  values remain relatively stable. This observation indicates that the initial  $^{87}\text{Sr}/^{86}\text{Sr}$  values of sphalerite, galena, and pyrite remain essentially unchanged during their growth, lending geological significance to the derived isochron ages, and effectively representing the primary mineralization age. The fundamental premise of Sm-Nd isochron dating for hydrothermal minerals is homogeneity, contemporaneity, and closure of the isotopic system. To ensure the basic conditions of contemporaneity and homogeneity of all samples, in this study, the samples were carbonates associated with the ore sulfides of the main ore-forming stage (mineralization Stages I and II). Additionally, there is no linear relationship between  $1/\text{Nd}$  and  $^{143}\text{Nd}/^{144}\text{Nd}$  (Figure 11b), indicating that the isochron formed by the nine data points (Figure 11a) has practical significance and could represent the primary ore-forming age.

The isochron ages of sulfides Rb-Sr ( $211.6 \pm 2.6$  Ma, Figure 10a) and carbonates Sm-Nd ( $211 \pm 4$  Ma, Figure 11a) are closely consistent within the error range, indicating that the main mineralization stage of the Dongtangzi Pb-Zn deposit occurred at about 211 Ma; that is, during the Late Triassic period.

The ages of some Zn-Pb and Au deposits in the Fengtai ore cluster have been reported. For instance, the Bafangshan–Erlihe Zn-Pb-Cu deposit has yielded a pyrite Re-Os isochron age of  $226 \pm 17$  Ma [90] and a sphalerite Rb-Sr isochron age of  $220.7 \pm 7.3$  Ma [91]. A quartz  $^{40}\text{Ar}-^{39}\text{Ar}$  isochron age of  $222.1 \pm 3.5$  Ma [92], a muscovite  $^{40}\text{Ar}-^{39}\text{Ar}$  age of  $209.5 \pm 1.4$  Ma, and Sm-Nd isochron ages of 209–208 Ma [93] have been obtained for the large Baguamiao gold deposit. Moreover, a sphalerite Rb-Sr isochron age of  $210.2 \pm 2.4$  Ma [23] has been determined for the Chaima gold deposit. In addition, to the west of the Fengtai ore cluster, the giant Changba–Lijiagou Pb-Zn deposit has a sulfide Rb-Sr isochron age of  $222.3 \pm 2.2$  Ma [77]. The large Liba gold deposit has yielded a mica  $^{40}\text{Ar}-^{39}\text{Ar}$  age of  $216.4 \pm 1.5$  Ma [94].

Similar ages have been obtained from the igneous rocks of the Fengtai ore cluster. For example, the NWW-trending granite porphyry dike of the Dongtangzi deposit has yielded a zircon U-Pb age of  $221.3 \pm 1.4$  Ma [25]; the granite porphyry dike and the NE-trending diorite dikes crosscutting the main orebody of the Bafangshan–Erlihe deposit and those within the mine area have yielded zircon U-Pb ages of  $217.9 \pm 4.5$  Ma and  $221 \pm 3$  Ma [21], respectively. Furthermore, the monzonitic granite and granodiorite of the Xiba pluton (Figure 1c) yielded zircon U-Pb ages of  $219 \pm 1$  Ma and  $218 \pm 1$  Ma, respectively [95]. The ages of the Taibai and Baoji plutons to the north of the Fengtai ore cluster are 216 Ma [96] and 216 to 210 Ma [97], respectively. The main ages of the west Qinling magmatic belt lie within a similar age range of approximately 220 Ma to 205 Ma [63,98]. In summary, the ages of the polymetallic deposits in west Qinling range from 231 to 197 Ma and are concentrated at around 220–200 Ma. On the other hand, the ages of the magmatic rocks range from 248 to 195 Ma and are concentrated at around 230–200 Ma [16].

The ages described above indicate that the Zn-Pb metallogenic events, magmatic activities, and regional tectonic processes of the west Qinling orogenic belt are consistent in time [23,99] and are closely related to the collisional processes that occurred between the Qinling micro-block and the Yangtze block along the Mianlue suture zone during the Late Triassic to Middle Jurassic periods [99,100].

### 6.3. Ore Genesis

As mentioned above, the M-shaped anticline structure hosting the Dongtangzi Zn-Pb deposit could be regarded as the first-order ore-controlling factor. Structural deformation, hydrothermal fracture filling, hydrothermal replacement mineralization, and intense wall rock alteration occurred after sedimentation and diagenesis. Additionally, the foreland basin environment that formed the ore-hosting Devonian carbonate and clastic rocks [55] is

totally different from that of the SEDEX Pb-Zn deposits in the world, which formed in intra- and/or epicratonic rifts and passive margin environments [71,101]. Therefore, the Zn-Pb enrichment in this area should be dominated by epigenetic hydrothermal mineralization rather than syngenetic exhalative sedimentary processes.

By combining the results of the Rb-Sr and Sm-Nd chronology and in situ S-Pb isotopic research conducted in this study, the genesis of the Dongtangzi Zn-Pb deposit can be attributed to epigenetic hydrothermal fluid processes driven by Late Triassic regional tectono-magmatic activities. This work has promising implications for our understanding of the analogous Zn-Pb deposits of the west Qinling orogenic belt, given their similar geological settings and metallogenic characteristics.

## 7. Conclusions

The in situ S-Pb isotopic analysis of sulfides from different episodes indicates that the sulfur and Zn-Pb of the Dongtangzi Zn-Pb deposit originated from mixed sources of magmatic fluid and regional metamorphic basement via TSR reaction.

The Stage I ore sulfides and the associated carbonate minerals yielded Rb-Sr and Sm-Nd isochron ages of  $211.6 \pm 2.6$  Ma and  $211 \pm 4$  Ma, respectively.

The Dongtangzi Zn-Pb deposit is an epigenetic hydrothermal deposit driven by Late Triassic regional tectono-magmatic activities, corresponding with the collisional processes that occurred between the Qinling micro-block and the Yangtze block along the Mianlue suture zone.

**Author Contributions:** Investigation, Q.H., Y.W., S.C., R.W. (Ran Wei), X.L., C.W., M.T. and W.W.; data curation, Q.H., Y.W. and J.L.; writing—original draft preparation, Q.H. and Y.W.; writing—review and editing, Y.W. and Q.H.; project administration, R.W. (Ruiting Wang) and W.G. All authors have read and agreed to the published version of the manuscript.

**Funding:** This work was funded by the Ministry of Science and Technology of China (2016YFC0600106), the National Sciences Foundation of China (41372089), and the Fundamental Research Funds for the Central Public Welfare Research Institutes (K1607).

**Data Availability Statement:** Data that support the findings of this study are available from the corresponding author upon reasonable request.

**Acknowledgments:** We are grateful to the Baoji No.717 Corps Limited of Northwest Nonferrous Geological and Mining Group for their enthusiastic help with the field work. Thanks to the editors for their efforts and important advice. Many thanks to the three anonymous reviewers and the Academic Editor for their careful comments and constructive suggestions.

**Conflicts of Interest:** The authors declare that this study received funding from Ministry of Science and Technology of China, the National Sciences Foundation of China, and the Fundamental Research Funds for the Central Public Welfare Research Institutes. The funders were not involved in the study design, collection, analysis, interpretation of data, the writing of this article or the decision to submit it for publication. Ruiting Wang, Weihong Gao, Changan Wang, Minjie Tang and Wentang Wu are employees of Northwest Nonferrous Geological and Mining Group Co., Ltd. The paper reflects the views of the scientists and not the company.

## References

1. Wang, R.T.; Wang, T.; Gao, Z.J.; Chen, E.H.; Liu, L.X. The main metal deposits metallogenic series and exploration direction in Feng-Tai Ore Cluster Region, Shaanxi Province. *West. Geol.* **2007**, *40*, 77–84. (In Chinese with English Abstract)
2. Li, J.H. Analysis on ore-controlling factors and prospecting potential of the Baguamiao-type gold deposits in Fengtai area, Shaanxi. *Miner. Resour. Geol.* **2008**, *22*, 62–64. (In Chinese with English Abstract)
3. Wu, X.D.; Song, S.K.; Gao, W.H.; Yang, S.W.; Zhang, X.G. Geological Characteristics and Prospecting Direction of Lead-Zinc Mine in Shaanxi Qiandongshan-Dongtangzi. *Gansu Metall.* **2016**, *38*, 87–94. (In Chinese with English Abstract)
4. Zhang, F.X. Characteristics and geological significance of the strawberry-like sulfide mineral in the lead-zinc deposit of Qian-dongshan and Yinmusi in Shaanxi province. *Geol. Prospect.* **1986**, *22*, 40–42.
5. Wang, J.L.; He, B.C.; Li, J.Z.; He, D.R. *Qinling-Type Lead-Zinc Ore Deposits in China*; Geological Publishing House: Beijing, China, 1996; pp. 116–145. (In Chinese with English Abstract)

6. Wang, Y.T.; Hu, Q.Q.; Wang, R.T.; Gao, W.H.; Chen, S.C.; Wei, R.; Wang, C.A.; Wen, B.; Wen, S.W.; Tang, M.J. A new metallogenic model and its significance in search for Zn-Pb deposits in Fengtai (Fengxian-Taibai) polymetallic ore concentration area, Shaanxi Province. *Miner. Deposits* **2020**, *39*, 587–606. (In Chinese with English Abstract)
7. Fang, W.X. Research on mineral geochemistry of Qiandongshan Lead-Zinc deposit, a large-sized deposit in Fengxian County, Shaanxi. *Acta Mineral. Sinica* **1999**, *19*, 198–205. (In Chinese with English Abstract)
8. Fang, W.X. Characteristics of sedimentary facies of hydrothermal for the giant Qiantongshan Lead-zinc ore deposit, Feng County, Shanxi Province. *Acta Sedimentol. Sinica* **1999**, *17*, 44–50. (In Chinese with English Abstract)
9. Huang, Z.Y.; Lu, R.A. Zoning characteristics and index of primary geochemical anomalies in Qiandongshan Pb-Zn deposit Shaanxi Province, China. *Geol. Prospect.* **2003**, *39*, 39–44. (In Chinese with English Abstract)
10. Ren, P.; Liang, T.; Liu, K.L.; Niu, L.; Lu, L.; Zhang, W.J. Geochemistry of Sulfur and Lead Isotopic Compositions of Sedex Lead-zinc Deposits in Fengtai Mineral Cluster Region of Qinling Mountains. *Northwest. Geol.* **2014**, *47*, 137–149. (In Chinese with English Abstract)
11. Zhang, G.L.; Tian, T.; Wang, R.T.; Gao, W.H.; Chang, Z.D. S, Pb isotopic composition of the Dongtangzi Pb–Zn deposit in the Fengtai ore concentration area of Shaanxi Province for tracing sources of ore-forming materials. *Geol. China* **2020**, *47*, 472–484. (In Chinese with English Abstract)
12. Li, H. Sulfides typomorphism and genesis of the Qiandongshan Pb-Zn deposit in Feng Country. *Geol. Prospect.* **1986**, *22*, 36–41. (In Chinese)
13. Yang, X.K. Comments on the genesis of the Qiandongshan Pb-Zn deposit in Fengtai area, Qinling. *Northwest Geol.* **1991**, *4*, 52–55. (In Chinese)
14. Li, J.Z.; He, D.R.; Wu, J.M. The Qinling-type Lead and Zinc ore deposit. *Acta Geol. Sinica* **1992**, *66*, 257–268.
15. Qi, S.J.; Li, Y. *The Types and Ore-Controlling Factors of Lead-Zinc Deposits in the Devonian Metallogenic Belt of Qinling Mountain*; Geological Publishing House: Beijing, China, 1993; pp. 1–178. (In Chinese with English Abstract)
16. Wang, Y.T.; Mao, J.W.; Hu, Q.Q.; Wei, R.; Chen, S.C. Characteristics and Metallogeny of Triassic polymetallic mineralization in Xicheng and Fengtai ore cluster zones, west Qinling, China and their implications for prospecting targets. *J. Earth Sci. Environ.* **2021**, *43*, 409–435. (In Chinese with English Abstract)
17. Shi, Y.H.; Wang, Y.; Chen, B.L.; Tan, R.W.; Gao, Y.; Shen, J.H. Characteristics of silicon-calcium surface ore-controlling in Fengtai ore-concentration areas, West Qinling Mountains: Examples from Qiandongshan Pb-Zn deposit. *Geol. China* **2022**, *49*, 226–240. (In Chinese with English Abstract)
18. Hu, Q.Q.; Wang, Y.T.; Mao, J.W.; Liu, X.L.; Chen, S.C.; Wei, R.; Zhang, J.; Wang, R.T.; Wang, C.A.; Dai, J.Z.; et al. Genesis of the Bafangshan-Erlihe Zn-Pb-Cu deposit in the Fengxian-Taibai ore cluster, west Qinling, China: Evidence from ore geology and ore-forming fluids. *Ore Geol. Rev.* **2020**, *126*, 103734. [[CrossRef](#)]
19. Wang, X.; Tang, R.Y.; Li, S.; Li, Y.X.; Yang, M.J.; Wang, D.S.; Guo, J.; Liu, P.; Liu, R.D.; Li, W.Q. *Qinling Orogeny and Metallogenesis*. Metallurgical Industry Press: Beijing, China, 1996; pp. 187–230. (In Chinese with English Abstract)
20. Zhang, F.X.; Wang, J.F. The submarine volcanic-exhalative-sedimentary origin of Lead-Zinc deposits in the Fengtai ore field, Shaanxi. *Geol. Rev.* **1988**, *34*, 157–168. (In Chinese with English Abstract)
21. Hu, Q.Q. *The Mineralization Features, Mechanism and Metallogenic Regularity of the Fengtai Pb-Zn Polymetallic Ore Cluster in West Qinling*. Ph.D. Thesis, Chinese Academy of Geological Sciences, Beijing, China, 2015.
22. Zhang, G.W.; Cheng, S.Y.; Guo, A.L.; Dong, Y.P.; Lai, S.C.; Yao, A.P. Mianlue paleo-suture on the southern margin of the Central Orogenic System in Qinling-Dabie— with a discussion of the assembly of the main part of the continent of China. *Geol. Bull. China* **2004**, *23*, 846–852. (In Chinese with English Abstract)
23. Wang, Y.T.; Liu, X.L.; Hu, Q.Q.; Zhang, J.; Chen, S.C.; Wang, R.T.; Dai, J.Z.; Gao, W.H.; Wen, S.W.; Chen, M.S.; et al. Rb-Sr isotopic Dating of Vein-like Sphalerites from the Chaima Au Deposit in Fengxian-Taibai Ore-concentration Area, Shaanxi Province and Its Geological Significance. *Northwest. Geol.* **2018**, *51*, 121–132. (In Chinese with English Abstract)
24. Wang, R.; Pang, Z.; Li, Q.; Zhang, G.; Zhang, J.; Cheng, H.; Wu, W.; Yang, H. Metallogenic Model and Prospecting Progress of the Qiandongshan–Dongtangzi Large Pb-Zn Deposit, Fengtai Orefield, West Qinling Orogeny. *Minerals* **2023**, *13*, 1163. [[CrossRef](#)]
25. Chen, S.C.; Wang, Y.T.; Yu, J.J.; Hu, Q.Q.; Zhang, J.; Wang, R.T.; Gao, W.H.; Wang, C.A. Petrogenesis of Triassic granitoids in the Fengxian–Taibai ore cluster, Western Qinling Orogen, central China: Implications for tectonic evolution and polymetallic mineralization. *Ore Geol. Rev.* **2020**, *123*, 103577. [[CrossRef](#)]
26. Zeng, L.G.; Zhang, J.; Hu, P. Spatio-temporal structure of the mineralization for Fengtai lead-zinc mineral cluster region, Shaanxi. *Geol. Sci. Technol. Inf.* **2009**, *28*, 84–90.
27. Lu, R.S.; Wei, H.M. Characteristics and Genesis of the Silicalites in Hot-Water Sedimentary Lead-Zinc Deposits in the Qinling Mountains. *Acta Petrol. Mineral.* **1992**, *11*, 14–21. (In Chinese with English Abstract)
28. Fang, W.X. Geochemical anomaly pattern and metallogenic model of the Bafangshan polymetallic deposit, Shaanxi. *Geol. Explor. Non-Ferrous Metals* **1997**, *6*, 167–171. (In Chinese with English Abstract)
29. Fu, J.L.; Hu, Z.C.; Zhang, W. In Situ Sulfur Isotopes ( $\delta^{34}\text{S}$  and  $\delta^{33}\text{S}$ ) Analyses in Sulfides and Elemental Sulfur Using High Sensitivity Cones Combined with the Addition of Nitrogen by Laser Ablation MC-ICP-MS. *Anal. Chim. Acta* **2016**, *911*, 14–26. [[CrossRef](#)]
30. Zhu, Z.Y.; Cook, N.J.; Yang, T.; Ciobanu, C.L.; Zhao, K.D.; Jiang, S.Y. Mapping of sulfur isotopes and trace elements in sulfides by LA-(MC)-ICP-MS: Potential analytical problems, improvements and implications. *Minerals* **2016**, *6*, 14. [[CrossRef](#)]

31. Zhu, Z.Y.; Jiang, S.Y.; Ciobanu, C.L.; Yang, T.; Cook, N.J. Sulfur isotope fractionation in pyrite during laser ablation: Implications for laser ablation multiple collector inductively coupled plasma mass spectrometry mapping. *Chem. Geol.* **2017**, *450*, 223–234. [[CrossRef](#)]
32. Ding, T.; Valkiers, S.; Kipphardt, H.; De Bievre, P.; Taylor, P.; Gonfiantini, R.; Krouse, R. Calibrated sulfur isotope abundance ratios of three IAEA sulfur isotope reference materials and V-CDT with a reassessment of the atomic weight of sulfur. *Geochim. Cosmochim. Acta* **2001**, *65*, 2433–2437. [[CrossRef](#)]
33. Chen, K.Y.; Yuan, H.L.; Bao, Z.A. Accurate and precise in situ determination of lead isotope ratios in NIST, USGS, MPI-DING and CGSG reference glasses using femtosecond laser ablation MC-ICP-MS. *Geostand. Geoanal. Res.* **2014**, *38*, 5–21.
34. Yuan, H.L.; Yin, C.; Chen, K.Y.; Bao, Z.A.; Zong, C.; Dai, M.N.; Lai, S.C.; Wang, R.; Jiang, S.Y. High precision in-situ Pb isotopic analysis of sulfide minerals by femtosecond laser ablation multicollector inductively coupled plasma mass spectrometry. *Sci. China Earth Sci.* **2015**, *58*, 1713–1721. [[CrossRef](#)]
35. Bao, Z.A.; Lu, C.; Zong, C.L.; Yuan, H.L.; Chen, K.Y.; Dai, M.N. Development of pressed sulfide powder tablets for in situ sulfur and lead isotope measurement using LA-MC-ICP-MS. *Int. J. Mass Spectrom.* **2017**, *421*, 255–262. [[CrossRef](#)]
36. Wang, Y.X.; Gu, L.X.; Zhang, Z.Z.; Wu, C.Z.; Zhang, K.J.; Li, H.M.; Yang, J.D. Geochronology and Nd–Sr–Pb isotopes of the bimodal volcanic rocks of the Bogda rift. *Acta Petrol. Sinica* **2006**, *22*, 1215–1224. (In Chinese with English Abstract)
37. Wang, Y.X.; Yang, J.D.; Chen, J.; Zhang, K.J.; Rao, W.B. The Sr and Nd isotopic variations of the Chinese Loess Plateau during the past 7Ma: Implications for the East Asian winter monsoon and source area of loess. *Palaeogeogr. Palaeoclimatol. Palaeoecol.* **2007**, *249*, 351–361. [[CrossRef](#)]
38. Ludwig, K.R. User's Manual for Isoplot 3.70. A Geochronological Toolkit for Microsoft Excel. *Berkeley Geochronol. Center Spec. Publ.* **2008**, *4*, 1–74.
39. Li, W.B.; Huang, Z.L.; Xu, D.R.; Cheng, J.; Xu, C.; Guan, T. Rb–Sr Isotopic method on Zinc-Lead ore deposits: A review. *Geotecton. Metall.* **2002**, *26*, 436–441. (In Chinese with English Abstract)
40. Ohmoto, H. Systematics of sulfur and carbon isotopes in hydrothermal ore deposits. *Econ. Geol.* **1972**, *67*, 551–578. [[CrossRef](#)]
41. Ohmoto, H.; Rye, R.O. Isotopes of sulfur and carbon. In *Geochemistry of Hydrothermal Ore Deposits*; Barnes, H.L., Ed.; Wiley: New York, NY, USA, 1979; pp. 509–567.
42. Wilkin, R.T.; Barnes, H.L. Pyrite formation by reactions of iron monosulfides with dissolved inorganic and organic sulfur species. *Geochim. Cosmochim. Acta* **1996**, *60*, 4167–4179. [[CrossRef](#)]
43. Jørgensen, B.B. A theoretical model of the stable sulfur isotope distribution in marine sediments. *Geochim. Cosmochim. Acta* **1979**, *43*, 363–374. [[CrossRef](#)]
44. Ohmoto, H. Biogeochemistry of sulfur and the mechanisms of sulfide–sulfate mineralization in Archean oceans. In *Early Organic Evolution: Implications for Mineral and Energy Resources*; Schidlowski, M., Golubic, S., Kimberley, M.M., Mckirdy, D.M., Trudinger, P.A., Eds.; Springer: Berlin, Germany, 1992; pp. 378–397.
45. Wei, H.M.; Lu, R.S. An exploratory study of the source of mineralized materials in the stratabound Pb–Zn–(Cu) ore deposits of the Fengtai ore field in the Qinling Mountains. *J. Xi'an Coll. Geol.* **1990**, *12*, 28–39.
46. Ren, P. Occurrence State and Enrichment Mechanism of Dispersed Elements in Typical Lead-Zinc Deposits of Shaanxi. Master's Thesis, Chang'an University, Xi'an, China, 2013; pp. 1–69.
47. Claypool, G.E.; Holser, W.T.; Kaplan, I.R.; Hitoshi, S.; Zak, I. The age curves of sulfur and oxygen isotopes in marine sulfate and their mutual interpretation. *Chem. Geol.* **1980**, *28*, 199–260. [[CrossRef](#)]
48. Wilkinson, J.; Hitzman, M. The Irish Zn–Pb ore field: The view from 2014. In *Irish Association for Economic Geology: Current Perspectives on Zinc Deposits*; Irish Association for Economic Geology: Dublin, UK, 2014; pp. 59–72.
49. Slack, J.F.; Dumoulin, J.A.; Schmidt, J.M.; Young, L.E.; Rombach, C.S. Paleozoic sedimentary rocks in the Red Dog Zn–Pb–Ag district and vicinity, western Brooks Range, Alaska: Provenance, deposition, and metallogenic significance. *Econ. Geol.* **2004**, *99*, 1385–1414. [[CrossRef](#)]
50. Zheng, Y.F.; Chen, J.F. *Steady Isotope Geochemistry*; Science Publishing House: Beijing, China, 2000; pp. 1–64. (In Chinese)
51. Kiyosu, Y.; Krouse, H.R. The role of organic acid in the abiogenic reduction of sulfate and the sulfur isotope effect. *Geochem. J.* **1990**, *24*, 21–27. [[CrossRef](#)]
52. Machel, H.G.; Krouse, H.R.; Sassen, R. Products and distinguishing criteria of bacterial and thermochemical sulfate reduction. *Appl. Geochem.* **1995**, *10*, 373–389. [[CrossRef](#)]
53. Fry, B.; Gest, H.; Hayes, J.M. Sulfur isotope effects associated with protonation of HS<sup>−</sup> and volatilization of H<sub>2</sub>S. *Chem. Geol. Isot. Geosci. Sec.* **1986**, *58*, 253–258. [[CrossRef](#)]
54. Holser, W.T.; Kaplan, I.R. Isotope geochemistry of sedimentary sulfates. *Chem. Geol.* **1966**, *1*, 93–135. [[CrossRef](#)]
55. Dong, Y.P.; Santosh, M. Tectonic architecture and multiple orogeny of the Qinling orogenic Belt, Central China. *Gondwana Res.* **2016**, *29*, 1–40. [[CrossRef](#)]
56. Zheng, W.Z.; Cao, Z.Q.; Wei, Z.; Liu, Z.M.; Xu, S.K.; Deng, X.L. The characteristics, genesis and prospecting significance of “salt-soluble breccia” of Lower Middle Triassic in southern Shaanxi Province. *Geol. Chem. Miner.* **1988**, *2*, 37–43. (In Chinese)
57. Yang, B.; Tan, Y.T. Analysis of metallogenic regularity and prospecting potential of non-metallic minerals in Shaanxi Province. *China Non-Metall. Miner. Ind.* **2018**, *132*, 7–10. (In Chinese)

58. Carr, G.R.; Dean, J.A.; Suppel, D.W.; Heithersay, P.S. Precise lead isotope fingerprinting of hydrothermal activity associated with Ordovician to Carboniferous metallogenic events in the Lachlan fold belt of New South Wales. *Econ. Geol.* **1995**, *90*, 1467–1505. [[CrossRef](#)]
59. Muchez, P.; Heijlen, W.; Banks, D.; Blundell, D.; Boni, M.; Grandia, F. Extensional tectonics and the timing and formation of basin-hosted deposit in Europe. *Ore Geol. Rev.* **2005**, *27*, 241–267. [[CrossRef](#)]
60. Pass, H.E.; Cooken, D.R.; Davidson, G.; Maas, R.; Dipple, G.; Rees, C.; Ferreira, L.; Tayler, C.; Deyell, C.L. Isotope geochemistry of the northeast zone, Mount Polley alkali Cu-Au-Ag porphyry deposit, British Columbia: A case for carbonate assimilation. *Econ. Geol.* **2014**, *109*, 859–890. [[CrossRef](#)]
61. Zhou, J.X.; Wang, X.C.; Wilde, S.A.; Luo, K.; Huang, Z.L.; Wu, T.; Jin, Z.G. New insights into the metallogeny of MVT Zn-Pb deposits: A case study from the Nayongzhi in South China, using field data, fluid compositions, and in situ S-Pb isotopes. *Am. Mineral.* **2018**, *103*, 91–108. [[CrossRef](#)]
62. Zartman, R.E.; Haines, S.M. The plumbotectonic model for Pb isotopic systematics among major terrestrial reservoirs—A case for bi-directional transport. *Geochim. Cosmochim. Acta* **1981**, *52*, 1327–1339. [[CrossRef](#)]
63. Qin, J.F.; Lai, S.C.; Grapes, R.; Diwu, C.R.; Ju, Y.J.; Li, Y.F. Origin of Late Triassic high-Mg adakitic granitoid rocks from the Dongjiangkou area, Qinling orogen, central China: Implications for subduction of continental crust. *Lithos* **2010**, *120*, 347–367. [[CrossRef](#)]
64. Qin, J.F.; Lai, S.C.; Li, Y.F. Slab breakoff model for the Triassic post-collisional adakitic granitoids in the Qinling orogenic belt, central China: Zircon U-Pb ages, geochemistry and Sr-Nd-Pb isotopic constraints. *Int. Geol. Rev.* **2008**, *50*, 1080–1104. [[CrossRef](#)]
65. Qin, J.F.; Lai, S.C.; Wang, J.; Li, Y.F. Zircon LA-ICP MS U-Pb age, Sr-Nd-Pb isotopic compositions and geochemistry of the Triassic Wulong granodiorite (South Qinling, Central China) and their petrogenesis significance. *Acta Geologica Sinica* **2008**, *82*, 425–437.
66. Qin, J.F.; Lai, S.C.; Wang, J.; Li, Y.F. The high-Mg# adakite-like tonalites from Xichahe, South Qinling: Its petrogenesis and geological implication. *Int. Geol. Rev.* **2007**, *49*, 1145–1158.
67. Xia, L.Q.; Xia, Z.C.; Li, X.M.; Ma, Z.P.; Xu, X.Y. Petrogenesis of the Yaolinghe group, Wudang group volcanic rocks and basic dyke swarms from eastern part of the South Qinling Mountains. *Northwest Geology* **2008**, *41*, 1–29. (In Chinese with English Abstract)
68. Xia, L.Q.; Xia, Z.C.; Xu, X.Y.; Li, X.M.; Ma, Z.P. Petrogenesis of the Bikou Group volcanic rocks. *Earth Sci. Front.* **2007**, *14*, 84–101.
69. Xu, J.F.; Castillo, P.R.; Li, X.H.; Yu, X.Y.; Zhang, B.R.; Han, Y.W. MORB-type rocks from the Paleo-Tethyan Mian-Lueyang northern ophiolite in the Qinling Mountains, central China: Implications for the source of the low  $^{206}\text{Pb}/^{204}\text{Pb}$  and high  $^{143}\text{Nd}/^{144}\text{Nd}$  mantle component in the Indian Ocean. *Earth Planet. Sci. Lett.* **2002**, *198*, 323–337. [[CrossRef](#)]
70. Broadbent, G.C.; Myers, R.E.; Wright, J.V. Geology and origin of shale-hosted Zn-Pb-Ag mineralization at the Century deposit, northwest Queensland, Australia. *Econ. Geol.* **1998**, *93*, 1264–1294. [[CrossRef](#)]
71. Leach, D.L.; Sangster, D.; Kelley, K.; Large, R.R.; Garven, G.; Gutzmer, J.; Walters, S. Sediment-hosted lead-zinc deposits: A global perspective. *Econ. Geol.* **2005**, *100*, 561–607.
72. Liu, J.M.; Zhao, S.R.; Shen, J.; Jiang, N.; Huo, W.G. Review on direct isotopic dating of hydrothermal ore-forming processes. *Progress Geophys.* **1998**, *13*, 46–55. (In Chinese with English Abstract)
73. Nakai, S.; Halliday, A.N.; Kesler, S.E.; Jones, H.D.; Kyle, J.R.; Lane, T.E. Rb-Sr dating of sphalerites from Mississippi Valley (MVT) ore deposits. *Geochim. Cosmochim. Acta* **1993**, *57*, 417–427. [[CrossRef](#)]
74. Nakai, S.; Halliday, A.N.; Kesler, S.E.; Jones, H.D. Rb-Sr dating of sphalerites from Tennessee and the genesis of Mississippi Valley type ore deposits. *Nature* **1990**, *346*, 354–357. [[CrossRef](#)]
75. Zhang, R.B.; Liu, J.M.; Ye, J.; Chen, F.K. Chalcopyrite Rb-Sr isochron age dating and its ore-forming significance in Shouwangfen copper deposit, Hebei province. *Acta Petrol. Sinica* **2008**, *24*, 1353–1358. (In Chinese with English Abstract)
76. Zhang, C.Q.; Li, X.H.; Yu, J.J.; Mao, J.W.; Chen, F.K.; Li, H.M. Rb-Sr dating of single sphalerites from the Daliangzi Pb-Zn deposit, Sichuan, and its geological significances. *Geol. Rev.* **2008**, *54*, 532–538. (In Chinese with English Abstract)
77. Hu, Q.Q.; Wang, Y.T.; Mao, J.W.; Wei, R.; Liu, S.Y.; Ye, D.J.; Yuan, Q.H.; Dou, P. Timing of the formation of the Changba-Lijiagou Pb-Zn ore deposit, Gansu Province, China: Evidence from Rb-Sr isotopic dating of sulfides. *J. Asian Earth Sci.* **2015**, *103*, 350–359. [[CrossRef](#)]
78. Wang, J.; Duan, D.; Chen, X.; Kong, Z.; Zhang, C.; Zhou, J.; Wu, Y. Neoproterozoic Zn-Pb mineralization in the world-class Sichuan-Yunnan-Guizhou Zn-Pb triangle, southwest China: Insights from apatite geochemistry and in situ sericite Rb-Sr geochronology of the Daxiao deposit. *Ore Geol. Rev.* **2023**, *160*, 105569. [[CrossRef](#)]
79. Yu, H.; Gou, X.L.; Zhang, Y.C.; Dong, H.Y.; Tang, J.R.; Cui, Y.Y. Insights into ore genesis of the Beishan Pb-Zn deposit in Guangxi, South China: Evidence from Rb-Sr dating and in-situ S-Pb isotopes. *Ore Geol. Rev.* **2023**, *163*, 105779. [[CrossRef](#)]
80. Chen, C.; Lv, X.; Gun, M.; Yang, J. Metallogenic chronology and tectonic setting of the Erdaohe Pb-Zn-Ag deposit in Inner Mongolia, NE China: Constraints from sphalerite Rb-Sr dating, zircon U-Pb dating, and Hf isotope analysis. *Ore Geol. Rev.* **2021**, *134*, 104067. [[CrossRef](#)]
81. Yang, F.; Wang, G.; Cao, H.; Li, R.; Tang, L.; Huang, Y.; Zhang, H.; Xue, F.; Jia, W.; Guo, N. Timing of formation of the Hongdonggou Pb-Zn polymetallic ore deposit, Henan Province, China: Evidence from Rb-Sr isotopic dating of sphalerites. *Geosci. Front.* **2017**, *8*, 605–616. [[CrossRef](#)]
82. Rosa, D.; Schneider, J.; Chiaradia, M. Timing and metal sources for carbonate-hosted Zn-Pb mineralization in the Franklinian Basin (North Greenland): Constraints from Rb-Sr and Pb isotopes. *Ore Geol. Rev.* **2016**, *79*, 392–407. [[CrossRef](#)]

83. Zhou, J.; Huang, Z.; Yan, Z. The origin of the Maozu carbonate-hosted Pb–Zn deposit, southwest China: Constrained by C–O–S–Pb isotopic compositions and Sm–Nd isotopic age. *J. Asian Earth Sci.* **2013**, *73*, 39–47. [[CrossRef](#)]
84. Zhang, J.; Wen, H.; Qiu, Y.; Zhang, Y.; Li, C. Ages of sediment-hosted Himalayan Pb–Zn–Cu–Ag polymetallic deposits in the Lanping basin, China: Re–Os geochronology of molybdenite and Sm–Nd dating of calcite. *J. Asian Earth Sci.* **2013**, *73*, 284–295. [[CrossRef](#)]
85. Zhang, H.; Ji, W.; Yang, X.; Zhou, J.X.; Sun, C.; Jia, Z.; Hong, J.; Lv, P.; Zhao, Z.; Hou, Q. The origin of the Quemocuo carbonate-hosted Pb–Zn deposit in the Sanjiang Tethyan Belt, SW China: Constrained by Sm–Nd isochronic age and Sr–S–Pb isotope compositions. *Ore Geol. Rev.* **2020**, *117*, 103264. [[CrossRef](#)]
86. Xu, L.; Yang, J.H.; Zeng, Q.D.; Xie, L.W.; Zhu, Y.S.; Li, R.; Li, B. Pyrite Rb–Sr, Sm–Nd and Fe isotopic constraints on the age and genesis of the Qingchengzi Pb–Zn deposits, northeastern China. *Ore Geol. Rev.* **2020**, *117*, 103324. [[CrossRef](#)]
87. Halliday, A.N.; Shepherd, T.F.; Dickin, A.P.; Chesley, J.T. Sm–Nd evidence for the age and origin of a Mississippi Valley-type ore deposit. *Nature* **1990**, *344*, 54–56. [[CrossRef](#)]
88. Nie, F.J.; Bjorlykke, A.B.; Nilsen, K.S. The origin of the Proterozoic Bidjovagge gold–copper deposit, Finnmark, Northern Norway, as deduced from rare earth element and Nd isotope evidences on calcites. *Resour. Geol.* **1999**, *49*, 13–25. [[CrossRef](#)]
89. Pettke, T.; Diamond, L.W. Rb–Sr dating of sphalerite based fluid inclusion-host mineral isochrones: A certification of why it works. *Econ. Geol.* **1996**, *91*, 951–956. [[CrossRef](#)]
90. Zhang, F.; Liu, S.W.; Li, Q.G.; Sun, Y.L.; Wang, Z.Q.; Yan, Q.R.; Yan, Z. Re–Os and U–Pb Geochronology of the Erlihe Pb–Zn Deposit, Qinling orogenic belt, Central China, and constraints on its deposit genesis. *Acta Geol. Sinica* **2011**, *85*, 673–682. (In English) [[CrossRef](#)]
91. Hu, Q.Q.; Wang, Y.T.; Wang, R.T.; Li, J.H.; Dai, J.Z.; Wang, S.Y. Ore-forming time of the Erlihe Pb–Zn deposit in the Fengxian–Taibai ore cluster, Shaanxi Province: Evidence from the Rb–Sr isotopic dating of sphalerites. *Acta Petrol. Sinica* **2012**, *28*, 258–266. (In Chinese with English Abstract)
92. Feng, J.Z.; Wang, D.B.; Wang, X.M.; Shao, S.C.; Ma, Z.G.; Zhang, X.G. Geology and Metallogenesis of the Baguamiao Giant Gold Deposit in Fengxian, Shaanxi Province. *Acta Geol. Sinica* **2003**, *77*, 387–398. (In Chinese with English Abstract)
93. Wang, Y.T.; Mao, J.W.; Zhang, J.; Wang, R.T.; Chen, G.M.; Hu, Q.Q.; Chen, S.C.; Liu, X.L. Geochronological constraints on the Baguamiao gold deposit, West Qinling orogen, central China: Implications for ore genesis and geodynamic setting. *Ore Geol. Rev.* **2020**, *122*, 103508. [[CrossRef](#)]
94. Zeng, Q.T.; McCuaig, T.C.; Hart, J.R.; Jourdan, F.; Muhling, J.; Bagas, L. Structural and geochronological studies on the Liba goldfield of the West Qinling Orogen, Central China. *Miner. Depos.* **2012**, *47*, 799–819. [[CrossRef](#)]
95. Zhang, F.; Liu, S.W.; Li, Q.G.; Wang, Z.Q.; Han, Y.G.; Yang, K.; Wu, F.H. LA–ICP–MS zircon U–Pb geochronology and geological significance of Xiba Granitoids from Qinling, Central China. *Acta Sci. Nat. Univ. Pekin.* **2009**, *45*, 833–840. (In Chinese with English Abstract)
96. Zhang, H.F.; Zhang, L.; Harris, N.; Jin, L.L. U–Pb zircon ages, geochemical and isotopic compositions of granitoids in Songpan–Graze fold belt, eastern Tibetan Plateau: Constraints on petrogenesis and tectonic evolution of the basement. *Contrib. Mineral. Petrol.* **2006**, *152*, 75–88. [[CrossRef](#)]
97. Liu, S.W.; Yang, P.T.; Li, Q.G. Indosinian Granitoids and Orogenic processes in the Middle Segment of the Qinling Orogen, China. *J. Jilin Univ. Earth Sci. Ed.* **2011**, *41*, 1928–1943. (In Chinese with English Abstract)
98. Sun, W.D.; Li, S.G.; Ya, D.C.; Li, Y.J. Zircon U–Pb dating of granitoids from South Qinling, Central China and their geological significance. *Geochimica* **2000**, *29*, 209–216. (In Chinese with English Abstract)
99. Mao, J.W.; Zhou, Z.H.; Feng, C.Y.; Wang, Y.T.; Zhang, C.Q.; Peng, H.J.; Yu, M. A preliminary study of the Triassic large-scale mineralization in China and its geodynamic setting. *Geol. China* **2012**, *39*, 1437–1471. (In Chinese with English Abstract)
100. Mao, J.W.; Qiu, Y.M.; Goldfarb, R.J.; Zhang, Z.C.; Ren, F.S. Geology, distribution, and classification of gold deposits in the Western Qinling belt, Central China. *Miner. Depos.* **2002**, *37*, 352–377. [[CrossRef](#)]
101. Leach, D.L.; Marsh, E.; Emsbo, P.; Rombach, C.; Kelley, K.D.; Reynolds, J.; Anthony, M. Nature of hydrothermal fluids at the shale-hosted Red Dog Zn–Pb–Ag deposits, Brooks Range, Alaska. *Econ. Geol.* **2004**, *99*, 1449–1480. [[CrossRef](#)]

**Disclaimer/Publisher’s Note:** The statements, opinions and data contained in all publications are solely those of the individual author(s) and contributor(s) and not of MDPI and/or the editor(s). MDPI and/or the editor(s) disclaim responsibility for any injury to people or property resulting from any ideas, methods, instructions or products referred to in the content.